Seismic constraints on damage growth within an unstable hanging glacier

Małgorzata Chmiel[1], Fabian Walter[2], Antione Pralong[3], Lukas E Preiswerk[3], Martin Funk[4], Lorenz Meier[5], and Florent Brenguier[6]

[1]Swiss Federal Institute for Forest, Snow and Landscape Research
[2]Swiss Federal Institute for Forest, Snow and Landscape Research (WSL)
[3]ETH Zürich
[4]VAW
[5]Geopraevent Ltd.
[6]Institut des Sciences de la Terre, Univ. Grenoble Alpes.

December 7, 2022

Abstract

Forecasting of hanging glacier instabilities remains challenging as sensing technology focusing on the ice surface fail to detect englacial damage leading to large-scale failure. Here we combine icequake cluster analysis with coda wave interferometry constraining damage growth on Switzerland's Eiger hanging glacier before a 15,000m3 break-off event. The method focuses on icequake migration within clusters rather than previously proposed "event counting". Results show that one cluster originated from the glacier front and migrated by 13(+/- 4) m within five weeks before the break-off event. The corresponding crevasse extension separates unstable and stable ice masses. We use the measured source displacement for damage parametrization and find a 90% agreement between an analytical model based on damage mechanics and frontal flow velocities measured with an interferometric radar. Our analysis provides observational constraints for damage growth, which to date is primarily a theoretical concept for modeling englacial fractures.

Seismic constraints on damage growth within an unstable hanging glacier

Małgorzata Chmiel[1,2], Fabian Walter[1,2], Antoine Pralong[2], Lukas Preiswerk[2], Martin Funk[2], Lorenz Meier[3], Florent Brenguier[4]

[1]Swiss Federal Institute for Forest, Snow and Landscape Research WSL, Zürich, Switzerland
[2]Laboratory of Hydraulics, Hydrology and Glaciology (VAW), ETH Zürich, Zürich, Switzerland
[3]Geoprevent AG, Technoparkstrasse 1, Zürich, Switzerland
[4]Univ. Grenoble Alpes, Institut des Sciences de la Terre, Grenoble, France

Key Points:

- In the months leading up to a break-off event we find thousands of recurring icequakes on the Eiger hanging glacier in Switzerland.
- Coda wave interferometry resolves displacements of icequake multiplets.
- One multiplet displacement corresponds to crevasse extension separating unstable and stable ice masses, which represents englacial damage.

Corresponding author: Małgorzata Chmiel, `malgorzata.chmiel@wsl.ch`

Abstract

Forecasting of hanging glacier instabilities remains challenging as sensing technology focusing on the ice surface fail to detect englacial damage leading to large-scale failure. Here we combine icequake cluster analysis with coda wave interferometry constraining damage growth on Switzerland's Eiger hanging glacier before a 15,000 m^3 break-off event. The method focuses on icequake migration within clusters rather than previously proposed "event counting". Results show that one cluster originated from the glacier front and migrated by 13($\pm$4 m) within five weeks before the break-off event. The corresponding crevasse extension separates unstable and stable ice masses. We use the measured source displacement for damage parametrization and find a 90% agreement between an analytical model based on damage mechanics and frontal flow velocities measured with an interferometric radar. Our analysis provides observational constraints for damage growth, which to date is primarily a theoretical concept for modeling englacial fractures.

Plain Language Summary

Predicting the development of ice mass breaking off from the front of unstable glaciers is challenging. Such glaciers are often located in remote locations with steep terrain, making it difficult to instrument and gather observations. Because of that, our current understanding of ice damage development on unstable glaciers is limited. Here, we propose a new approach to tackle this problem using seismic observations from the Eiger hanging glacier in the Swiss Alps before a moderate 15,000 m^3 break-off event. We first group seismic signals according to their waveform similarity. We then use scattered arrivals to track displacement in seismic source locations. Our results suggest that a group of seismic signals is generated by crevasse propagation separating the unstable ice mass and the stable ice uphill. Combined with a simple analytical model, these observations indicate that seismic source displacement can be associated with damage propagation within the unstable glacier. This is an important step toward a better understanding of damage growth within unstable glaciers.

1 Introduction

Hanging glaciers are high-altitude glaciers that are inherently unstable and might produce catastrophic break-off events (Faillettaz et al., 2015). These glaciers are often partially frozen to their bedrock, allowing them to locate on steep slopes. Break-off events leading to substantial ice avalanches pose severe hazards to humans, settlements, and infrastructure in Alpine terrain worldwide (e.g., Faillettaz et al., 2015; Tian et al., 2017).

Timely warning and evacuation often remain the only solution to protect the population (Faillettaz et al., 2015). Good break-off forecasts are achieved with remote measurements of glacial surface velocities capturing a power-law acceleration before a break-off event (Flotron, 1977; Röthlisberger, 1977; Pralong & Funk, 2006; Faillettaz et al., 2008). However, the destabilization of large ice masses results from a combination of glacier geometry, ice rheology, damage evolution, and basal motion (Faillettaz et al., 2015). These controls cannot be revealed with measurements of ice surface velocities alone and require detection of englacial changes leading to crevasse grow (Pralong & Funk, 2006).

In the recent 1-2 decades, passive seismic measurements have been growing increasingly popular in glaciology (Podolskiy & Walter, 2016). They provide access to the interior and basal environments of glaciers and ice sheets: Crevasse dynamics, basal sliding, subglacial water flow, and iceberg detachment are notoriously difficult to study with conventional glaciological techniques but can be monitored with seismometers at the ice surface (for an overview see, e.g., Podolskiy and Walter (2016); Aster and Winberry (2017); Nanni et al. (2020)). For break-off events of steep glacial bodies, seismological research has so far focused on detecting icequakes. This term is often used to refer to glacier-related microseismic events generated by glacier (stick-)slip motion (Weaver & Malone, 1979; Caplan-Auerbach & Huggel, 2007) and crack opening (Faillettaz, Funk, & Sornette, 2011; Faillettaz et al., 2008; Preiswerk et al., 2016). Beyond "icequake counting", analysis on seismic event locations or waveform attributes could reveal further details of source mechanisms and thus help characterizing ice structural change leading to failure. This would allow testing theoretical predictions on the role of damage evolution (Pralong & Funk, 2006), basal sliding (Dalban Canassy et al., 2012; Allstadt & Malone, 2014; Dalban Canassy et al., 2013), and the role of external forcing mechanisms, in particular climatic nature (Faillettaz, Funk, & Sornette, 2011; Faillettaz, Sornette, & Funk, 2011).

Here, we study a hanging glacier's icequake signals focusing on later arriving seismic phases ('coda') to quantify fracture development behind the ice front before a break-off. We use seismic data from a 4-station network deployed on the Eiger hanging glacier in Switzerland between April and August 2016. We find over 200,000 recurring icequakes with substantial coda out of which we compile catalogs of 30 clusters each comprising events with high waveform similarities. Focusing on coda changes, we use the clusters for monitoring the relative source displacements that can be interpreted in terms of damage evolution within the ice, hence a preparation phase towards break-off events.

2 Study site

The Eiger hanging glacier, located on the west face of the Eiger summit, Switzerland, extends from 3,500 to 3,200 m a.s.l. with a surface slope of 20° at the terminus [Margreth et al. (2017), Figure 1A-B, Figure S1]. The surface area of the Eiger hanging glacier was 0.08 km^2 in 2016 (Huss et al., 2013) with a mean and maximum thickness of about 40 m, and 70 m, respectively. The only study that performed temperature measurements of the Eiger hanging glacier dates back to 1997 (Lüthi & Funk, 1997). Lüthi and Funk (1997) determined englacial temperatures ranging between -5° and 0° and an average glacier flow velocity of 7 m a^{-1}. The Eiger hanging glacier is polythermal, meaning that water coexists with glacier ice at the glacier base, except for the base of the frontal part, which is cold and entirely frozen to the bed Lüthi and Funk (1997). We refer the reader to Figure S1 and Text S1 in Supplemental Information (SI) for more details on the glacier's thermal regime. The glacier lies almost entirely in the accumulation zone, exhibiting a positive annual net surface balance. At the ice front, the glacier extent is limited by a topographic bedrock step, leading to a steep ice cliff from which periodic break-off events occur (Raymond et al., 2003; Margreth et al., 2017; Marchetti et al., 2021). Typical volumes of unstable ice mass are $< 10{,}000\,\mathrm{m}^3$. The resulting ice avalanches are large enough to endanger hiking paths, ski infrastructure, and the train line that leads to Jungfraujoch, one of Europe's major tourist destinations (Figure 1A). In April 2016, a significant crevasse was observed behind the glacier front, indicating an impending break-off event. On the morning of August 25, 2016, an ice mass of 15,000 m^3 broke off the hanging glacier (Figure S12). This was the largest break-off event since 1991 (Margreth et al., 2017). The ice avalanche missed the Eigergletscher train station and came to rest 1200 m vertically below the glacier (Figure 1A).

3 Instrumentation

To warn against the break-off events, a monitoring system has been installed next to the glacier since 2016, including an automatic camera (two photos per day of the glacier front, Figure S12) and an interferometric radar measuring the velocity of the glacier front (Meier et al., 2016), Figure 1A. Between April and September, 2016 the interferometric radar at the train station Eigergletscher recorded line-of-sight displacements of the glacier front. We measured glacier front velocities as the maximum ice front displacement on the radar image per hour (Figure 1D).

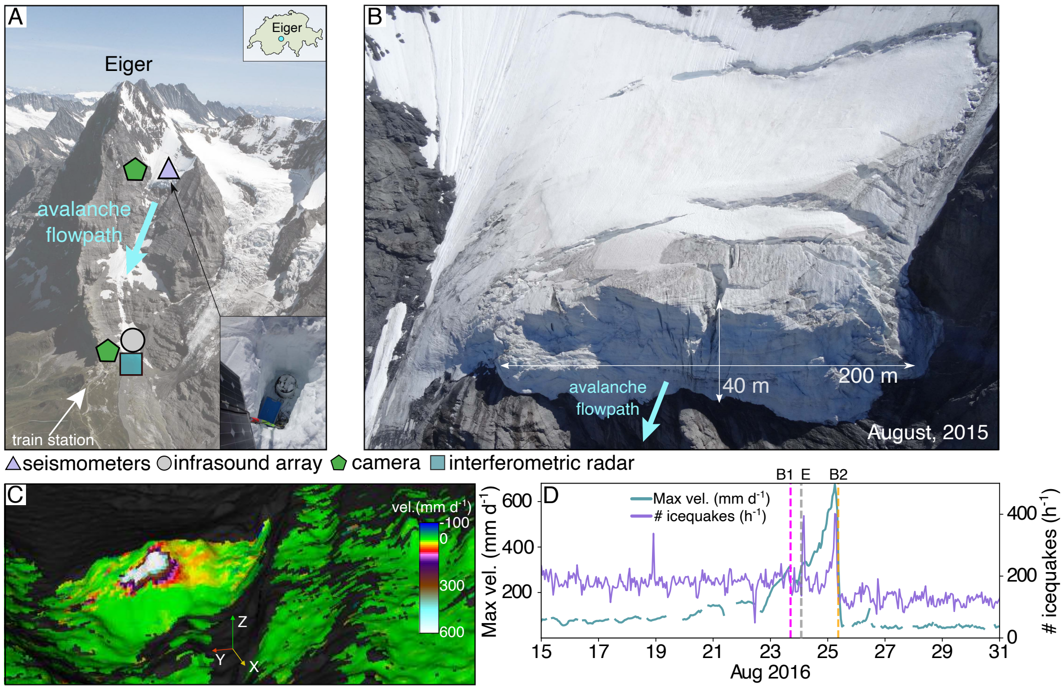

Figure 1. Study site: Eiger hanging glacier. (A) The following instruments were deployed on the glacier to monitor it: an infrasound array (gray circle, not operational during the break-off event), interferometric radar measuring glacier flow velocity (teal square), four 3-component seismometers (natural frequency: 1 Hz) installed on the glacier between April and August (stations EIG1-EIG4, purple triangles), an automatic camera photographing the unstable ice mass (green pentagons). Source: ETH-Bibliothek Zürich, Bildarchiv /Stiftung Luftbild Schweiz/ Photograph: Swissair Photo AG / LBS_R2-010615 / CC BY-SA 4.0. The upper inset shows the location of Mount Eiger in Switzerland. The lower inset shows one of the seismic stations installed on a granite plate for accurate leveling. The blue box contains the logger and battery. (B) The Eiger hanging glacier in August 2015. (C) The glacier flow velocity measured by the interferometric radar projected onto a digital elevation model (a zoom view on the glacier terminus, summed over 6 h, 02:01-08:01 UTC, August 25, 2016). (D). Temporal evolution of the maximum velocity of the glacier flow and an hourly icequake occurrence rate. Both curves are smoothed with a 1h-moving average. The time occurrences of a small (B1) and main break-offs (B2), and Amatrice earthquake (E, M 6.2) are represented in color-coded dashed vertical bars.

Between April and August 2016, we installed four 3C Lennartz seismometers (natural frequency 1 Hz) on the glacier to monitor its icequake activity [SED (1985) and see Preiswerk (2018) for details on acquisition]. Avalanches, snowfalls, and other factors associated with high altitude conditions strongly challenge instrument maintenance on the glacier. However, one station recorded continuously for 4.5 months (EIG2), and up to three seismic stations operated simultaneously (Figure 2B). Our seismic stations recorded the main break-off on August 25 together with a precursory event on August 23 and abundant icequake activity consisting of up to 400 events per hour (Figure 1D, 2B-C).

4 Methods

4.1 Analysis Overview: seismic repeaters, multiplets, and coda wave interferometry

We divided our icequake seismograms from the Eiger hanging glacier into clusters consisting of events with similar waveforms. In conventional seismological applications, waveform similarity is attributed to earthquake repeaters and multiplets that are closely-spaced events with nearly identical source mechanisms (Poupinet et al., 1984). The cross-correlation coefficient between two seismograms is a measure of similarity and ranges between -1 and 1 with the latter corresponding to a perfect match. Repeaters have been defined as waveform pairs with a cross-correlation coefficient >=0.9 (e.g., Uchida & Bürgmann, 2019). In glacial contexts, repeating icequakes have been linked to basal stick-slip beneath ice streams (Anandakrishnan & Bentley, 1993; Smith, 2006; Danesi et al., 2007; Zoet et al., 2012), Alpine valley glaciers (e.g., Helmstetter, Nicolas, et al., 2015; Walter et al., 2020; Gräff & Walter, 2021), and glacier-covered volcanoes [e.g., Thelen et al. (2013); Allstadt and Malone (2014)]. In contrast, multiplet seismograms have a lower cross-correlation coefficient >=0.5 and in glacial environments have been associated with a crevasse opening (Mikesell et al., 2012) and fracture propagation (Helmstetter, Moreau, et al., 2015).

Coda waves are the later arriving, multiply scattered seismic coda signals that sample the entire medium or its subvolume multiple times by following more complex and longer paths than the direct phases (Figure 2D). This increased sensitivity of coda waves is used in methods called "coda wave interferometry (CWI)" to measure subtle changes in source locations, perturbations in scatterer locations, and seismic velocities (e.g., Snieder et al., 2002; Curtis et al., 2006; Sens-Schönfelder & Brenguier, 2019). Source/scatterer and velocity perturbations leave different footprints on the coda as illustrated in Figure S10.

On Alpine glaciers, coda wave interferometry is challenging as homogeneous ice usually suppresses englacial scattering resulting in weak coda (e.g., Sergeant et al., 2020). However, on hanging glaciers like our study site, pervasive fracturing and multiple lateral reflections within small glacial basins generate substantial coda (Podolskiy & Walter, 2016). The seismograms of an icequake cluster at our study site confirm this with strong phase coherence of direct arrivals and pronounced changing coda (Figure 3A).

Here, we use CWI to determine changes in the separation of icequakes belonging to a single cluster (e.g., Snieder et al., 2002). This allows tracking the magnitude (not direction) of icequake cluster migration using a single station. For our icequake seismograms we assume that coda changes are driven by perturbations in source locations and/or in ice elastic properties rather than by perturbations in scattering crevasse fields. This assumption is based on moderate glacier flow velocity [$7\,\mathrm{m\,a^{-1}}$ Lüthi and Funk (1997)], on crevasse life times of up to 5 years which are large compared to the monitoring period (Colgan et al., 2016) and on high sensitivity of seismic velocities to changes in ice elasticity (Röthlisberger, 1972).

We can independently estimate changes in source locations and changes in the medium velocity (Singh et al., 2019). Velocity perturbation accumulate over the ray path leading to increasing travel time delays with increasing lapse time in the coda (Snieder et al., 2002; Singh et al., 2019). In contrast, when source position changes from the original to a perturbed location, some wave paths become longer while others become shorter and signals of these wave trajectories arrive earlier and later, respectively (Figure 2D). We thus use the variance of the travel time changes to determine source displacements (Snieder et al., 2002; Allstadt & Malone, 2014; Singh et al., 2019) (see Text S2 in SI for details).

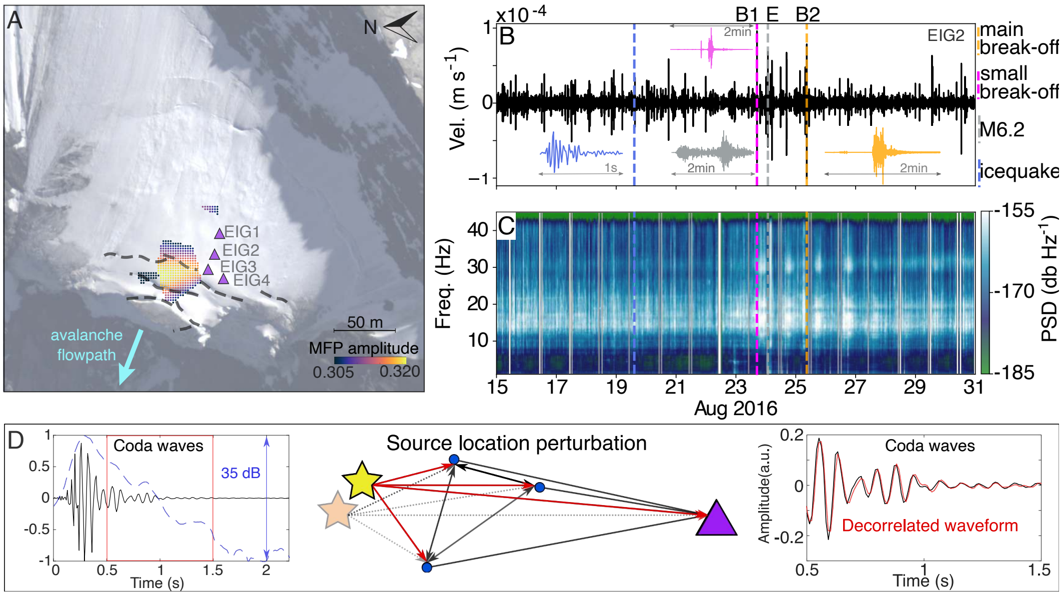

Figure 2. Seismic signals recorded at the Eiger hanging glacier. (A) Orthophoto of the Eiger hanging glacier one day after the main break-off event. The position of four seismic stations installed at the glacier is marked with purple triangles. The overlaid scatter plot shows the averaged cluster location with Matched-Field Processing. We average MFP results from 23 clusters and show only top 90% of the resulting MFP amplitude. Main crevasses are marked in black dashed lines. Photo source: swisstopo flight, line 1308201608260940, August 26, 2016. (B) Seismic signals recorded on the vertical component of the EIG2 station 10 days before and 5 days after the main break-off with a corresponding spectrogram in (C). The time occurrences of a single icequake, small and main break-offs, and Amatrice earthquake (M 6.2) are represented in dashed vertical bars and colors indicated in Figure 2B. (D) Left: Stack of icequakes within cluster 24 recorded at the vertical component of the EIG2 station. In red, we show the time window T_{min}=0.5 and T_{max}= 1.5 s that contains coda waves and in blue, the envelope decay in dB. Center: Illustration of a source location perturbation, with a source (star), receiver (triangle), and a medium with point scatterers (circles). Direct and scattered ray paths are marked in arrows: black and red (new ray paths). Right: Coda waveforms before (black) and after the source perturbation (red). Based on Figure 1 in Singh et al. (2019).

4.2 Catalog compilation

Prior to all processing, data are high-pass filtered at 1 Hz to focus on high-frequency signals related to glacier dynamics (Podolskiy & Walter, 2016). We first determine overall icequake activity using a short term average/long term average (STA/LTA) algorithm with coincidence trigger over all available stations [Allen (1978); see Text S2 in SI and Preiswerk (2018) for details]. Next, we identify clusters of events with similar waveforms by mutually cross-correlating STA/LTA detections within a sliding time window of 5 s using the Repeating Earthquake Detector in Python [RedPy, Hotovec-Ellis and Jeffries (2016)]. For this step we use coincidence triggers and cross-correlations on stations EIG2 and EIG4 between August 11 and 31, 2016.

We find over 200,000 repeating events with a correlation coefficient threshold of 0.9 from which we choose those clusters consisting of over 40 events, which amounts to 30 clusters (5 % of all clusters). To extend our analysis over the entire monitoring period, we construct template waveforms by stacking the icequake waveforms within each cluster. Next, we search for similar icequakes with template matching against the continuous data recorded at the EIG2 station (e.g., Gibbons & Ringdal, 2006). For the implementation, we use the correlation-based Fast Match Filter [FMF, Beaucé et al. (2018)], and we set the correlation coefficient threshold to 0.7. The threshold of 0.7 in the template detection with a single station provides a comprehensive catalog that we need for coda wave measurements while rejecting events that potentially originate from different clusters. These steps leave us with 36,989 icequakes from 30 clusters, which we refer to as "multiplets" even though some icequake pairs may share cross-correlation coefficients above 0.9.

4.3 Cluster location

We locate our clusters with Matched Field Processing [MFP, Baggeroer et al. (1993); Kuperman and Turek (1997)], which exploits cross-array signal coherence by calculating the cross-spectral correlation matrix [CSDM, Kuperman and Turek (1997)]. CSDM represents the coherence of the wavefield recorded at a group of sensors. Our four stations were never in operation simultaneously. Therefore for each cluster and station, we stack icequake waveforms recorded on the vertical component of the stations for periods when the station was working properly. This provides us with average waveform stacks for 2-4 stations depending on the cluster activity. We use a 1.5 s long time window taken form the beginning of the stack that includes the highest-amplitude phase, which for frequencies above 1 Hz we assume is a Rayleigh wave (Deichmann et al., 2000). We perform a 2D grid search over northing and easting with spatial increments of 1 m using a simple Rayleigh wave propagation model in a homogeneous medium ($\mathrm{v_R}$=1612 $\mathrm{ms^{-1}}$, optimized in the range of 1550-1700 $\mathrm{ms^{-1}}$ with a velocity increment of 10 $\mathrm{ms^{-1}}$).

For each cluster, the maximum amplitude of the normalized ambiguity map ("MFP amplitude", Figure S4) indicates the optimal source location that maximizes the fit between the CSDM of the waveform stacks and the model. We also produce an overlaid map reflecting the overall activity of 23 clusters (Figure 2A). For this, we stack the regions of the individual ambiguity maps that lie within 64 m ($\sim$ 1 wavelength) of each cluster's optimal source location. We exclude the source locations that localize at the grid border (7 clusters). See Chmiel et al. (2019); Bowden et al. (2020) and Text S2 for details.

4.4 Source displacements

We now focus on the separation between icequake multiplets in each cluster. In SI, Text S2, we furthermore estimate changes in the relative seismic velocity dv/v through CWI and the coda wave attenuation (Q_c^{-1}) by measuring the decay slope of the coda envelope based on the Aki and Chouet (1975) model. We first filter the seismograms of our 30 icequake clusters between 10 and 40 Hz and define a 1-s-long coda window starting at 0.5 s after the direct arrival associated with the surface wave (Figure 2D). To stabilize the measurement, we stack icequake signals within 4-hour windows after stacking up to 3 events per hour with the highest cross-correlation coefficient obtained from the template matching. As detailed in Section 4.1 we use CWI to measure a displacement between the centroid of icequake multiplets and invert for a continuous source displacement (Allstadt & Malone, 2014; Hotovec-Ellis & Jeffries, 2016). Since the measurements are not continuous, we use an L1 norm for regularization (e.g., Tibshirani, 1996; Chmiel et al., 2018) that enhances the solution sparsity.

5 Results

Between August 5 and the break-off event on August 25 the glacier front undergoes a clear acceleration from an average velocity of 4-5 cm day^{-1} to $>$ 60 cm day^{-1} (Figure 1D). After the main break-off on August 25, the velocity drops below 10 cm day^{-1}. We observe an increase in the overall (non-clustered) seismicity rate only ∼6 hours before the main break-off event (up to ∼400 events h^{-1}) and a drop to a lower level after the break-off (100 events h^{-1}). Before the small precursory break-off on August 23, seismicity did not increase notably. On the other hand, our results show elevated seismicity two hours after the passing of the teleseismic waves of the M 6.2 Amatrice earthquake (e.g., Chiaraluce et al., 2017), around 01:00 UTC on August 24. The two hour delay calls into question a direct relation to the earthquake's dynamic strain on the glacier ice. It does suggest that the detaching ice mass was still firmly attached, since the main break-off did not occur for another 31 hours. Another peak in seismic activity is visible on 18 August. On longer time scales, we observe recurrent 1-2 hour-long bursts of seismic activity that become ∼10 times more frequent after June 21 when the air temperature exceeds 0° C and surface melt takes place at the glacier (Figure S2).

24 out of the 30 clusters appear during the melt season. The clusters show the maximum activity 1-2 weeks before the break-off event and reduced activity after the break-off events. Nine clusters show decreasing activity after the break-off events, and three clusters are short-lived, appearing just before the minor break-off event between 12 and 22 August. The break-off events occur during a period of an elevated air temperature.

The averaged MFP analysis (Figure 2A) indicates clusters originating mainly from the glacier front and a location at the back of the glacier, likely associated with the "Bergschrund" separating flowing from stationary ice. 29 out of the 30 clusters follow a similar relative displacement trend with an average source displacement of 4 m (±1 m) from July 1 to August 31. Cluster 24, which locates near the glacier front, forms an exception, because its source displacement amounts to 13(±4 m). Between 10 and 40 Hz, the average source displacement within a single cluster is below 10 % of the shortest wavelengths of 40 m. This 10 % is well below the 30 % threshold at which CWI-derived displacements are accurate (Singh et al., 2019).

6 Discussion

(Faillettaz, Funk, & Sornette, 2011) showed that on another hanging glacier located in the Swiss Alps, Weisshorn glacier, the icequake activity accelerated together with the glacier front displacement ∼3 days before the failure of an unstable large ice mass (volume ∼120,000 m^3). Icequake activity reacts after the main break-off event on the Eiger hanging glacier, showing only half of the event rate compared to pre-break-off times. However, simple icequake detections are of little use for break-off forecasting since they increase only within a few hours prior to a break-off event or not at all (Figure 1D). The difference in icequake activity at Weisshorn and the Eiger hanging glacier might be related to different geometries, the thermal regime at the glacier bed, the type of instability, and the volume of break-off events. At the Weisshorn glacier, the damage growth near the steep cold glacier bed led to the failure. In contrast, at the Eiger hanging glacier, the instability development is also driven by the bedrock's geometry at the front of the glacier, which forces the opening of crevasses. (Pralong & Funk, 2006; Faillettaz et al., 2008).

For the present data set it is necessary to focus on specific icequake clusters, which present event groups with similar locations and fault mechanisms. To our knowledge, icequake clusters have not been previously reported on hanging glaciers. A central question is what their origins and the faulting mechanisms of the individual icequakes are. CWI reveals that most sources displaced by 4 m during two months, which is more than

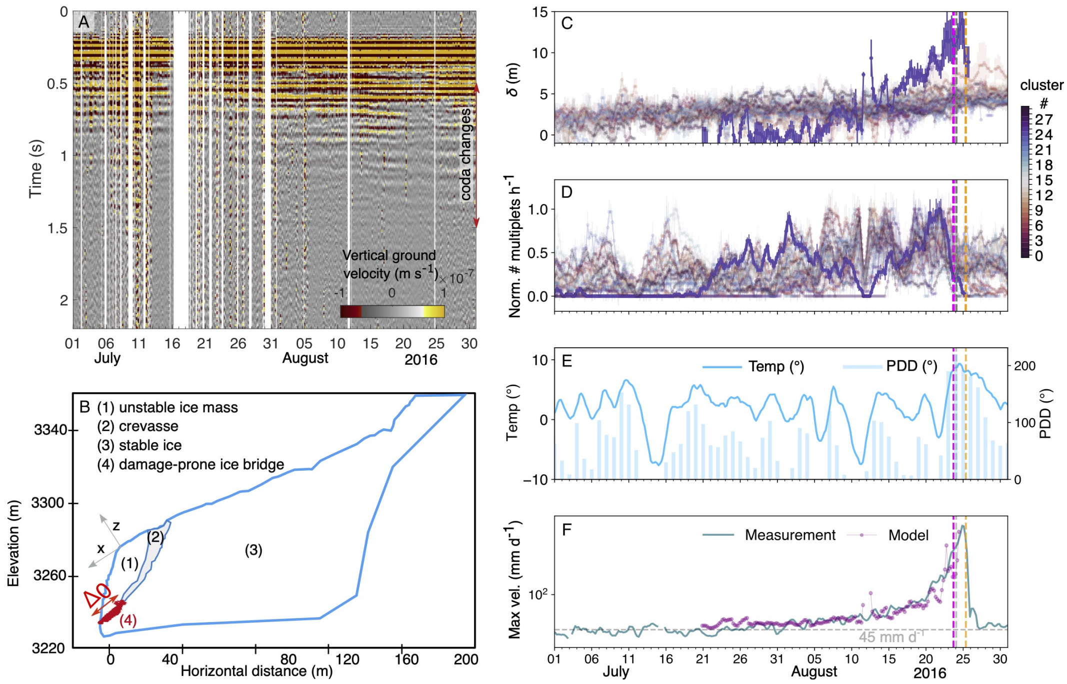

Figure 3. Icequake multiplets analysis and their displacement δ measured with coda wave interferometry. (A) Temporal variations of 4h-stacks of icequake multiplets recorded (vertical component of station EIG2 for cluster 3). Time (0.5-1.5) s used for CWI is marked with a red arrow. (B) Cartoon of the Eiger hanging glacier, after Pralong and Funk (2005). (C) Icequake multiplet centroid ("source") displacement δ and (D) icequake multiplets activity (normalized by the maximum number of events in the cluster). For each color-coded cluster, we represent the average source displacement over three components, and the errors are taken as the standard deviation from the average. In (D) the error bars are calculated as a standard deviation of the number of icequakes within 4 hours. (E) Air temperature measured at the MeteoSchweiz weather station Jungfraujoch. The temperature is corrected by $+1^\circ$ C to the altitude of Eiger hanging glacier, 3 km away. From the temperature time series we calculate Positive Degree values (PDD). PDD is the cumulative temperature above the melting point of 0° C over a given period (e.g., Wake & Marshall, 2015) and proportional to the amount of surface melt over a given period (e.g., Wake & Marshall, 2015). (F) Zoom on the maximum velocity of the glacier front measured with the interferometric radar (in teal) and the frontal velocity calculated with equation 2 (in purple). All measurements are smoothed with a 24-h moving average.

a factor of three faster than glacier bulk surface displacement (Lüthi & Funk, 1997) and thus cannot be explained exclusively by ice flow transporting englacial seismic sources. Instead, we propose that our cluster sources are extension events of crevasse tips. This explains an increase in cluster activity in spring when meltwater accumulates in crevasses and deepens them via hydrofracturing (e.g., Van der Veen, 1998). Alternatively, recurring icequakes have also been attributed to basal stick-slip events (e.g., Gräff & Walter, 2021). However, a displacement of stick-slip sources at 3-4 times the ice flow speed is difficult to argue given that the glacier front is frozen to the bed and thus not sliding (Lüthi & Funk, 1997).

Cluster 24 starts on July 18 and terminates its activity in the hours around the main break-off event (Figure 3C-D). We argue that this cluster corresponds to the crevasse separating the unstable ice mass (Figure 3B) involved in the major break-off and the stable ice uphill for the following reason: 1. The activity of cluster 24 ceases after the major break-off (Figure 3C, D). 2. MFP analysis locates cluster 24 towards the glacier front (Figure S4). 3. The source displacement of cluster 24 (marked in purple in Figure 3C) accelerates in parallel to the ice front velocity.

To explain this agreement between cluster displacement and front velocity quantitatively, we use the damage mechanics theory for ice rheology following Pralong et al. (2003). Damage D is a measure of the integrity of ice, with $D = 0$ and $D = 1$ representing undamaged and fully damaged ice, respectively. Damage is assumed to only affect the viscosity of ice, not its rheology, and softening of increasingly damaged ice through a critical damage accumulation at the glacier's basal shear zone explains the pre-break-off acceleration of the glacier front (Pralong, 2006b).

To link our cluster 24 centroid displacement to frontal velocities we propose that

$$D = \frac{\Delta}{\Delta_0} \tag{1}$$

where Δ is the source displacement within cluster 24 and Δ_0 is the maximum displacement before the break-off taken as 14 m. With equation 1 we parameterize the damage variable by the fraction of the ice connecting the unstable and stable glacier portions that is penetrated by the crevasse tip (Figure 3B). If this "ice bridge" is fully damaged, $\Delta = \Delta_0$ and hence $D = 1$, at which point the break-off occurs. We assume that D is measured towards the displacement direction ("x") and it does not depend on "z". Please see SI, Text S3 for an alternative damage parametrisation.

With the damage parameterization in equation 1, we can quantitatively model the frontal velocity (v_x) of the unstable ice mass in the flow direction "x" following Pralong (2006b):

$$v_x = CA\sigma_{xz}^n \left[\frac{\Delta H}{(1-D)^n} + \frac{H}{n+1} \right] \tag{2}$$

where σ_{xz} is the x^{th} and z^{th} entry of the stress tensor, A and n are the flow parameters (n is Glen's flow law exponent), H is the glacier thickness, ΔH is the active layer where damage develops, and C is an optimization constant to account for a geometrical difference from a parallel-sided slab geometry as assumed in equation 2. The first term of the equation describes the surface velocity due to the damage process, and the second one is the influence of the deformation of the ice column. We specify the values used in the inversion in Table S1 and refer the reader to SI Text and Pralong (2006b) for more details.

Glen's flow law exponent n is not well constrained with previously reported values ranging between $n = 1$ and $n = 4$ with a commonly assumed value of $n = 3$ and $A \sim 10^{-24}$ for non-damaged ice (Cuffey & Paterson, 2010). These values depend on temperature, water content, impurities, stress regime, and grain size (Cuffey & Paterson, 2010). We fit the equation 2 to the measured velocity optimizing for C and the exponent n (Figure 3F, Figure S8). The optimized value of the exponent is $n = 1.2$ and the numerical value of parameter C for equation 2 is of order 10^{14}.

The limitations of the Pralong (2006b) model might partially explain the large value of C. The assumed geometry of a very long parallel-sided used by Pralong (2006b) to derive the equation 2 is certainly an oversimplification for the motion of the front of the Eiger hanging glacier. The unstable frontal part of the Eiger hanging glacier experiences a tilting movement before the break-off. Therefore, the ice surface undergoes an accelerated motion, but the basal ice remains approximately at the same place. In SI, Test

S3, and Figure S9, we show an alternative analytical model without the parallel-sided slab assumption, and we show fit results to the more commonly used $n = 3$ using equation 2 (In SI Figure S8C, F).

The analytical model from equation 2 with optimized parameters agrees within 90 % with the measured velocity until 20 hours before the main break-off (Figure 3F). Afterward, the denominator of the first term in equation 2 results in a nonphysical divergence. These results indicate that, as opposed to monitoring glacier flow surface velocity which only indirectly measures englacial damage, seismology makes it possible to *directly* measure englacial damage. Finally, we note that the 14.0(±4m) displacement of cluster 24 is similar to the fracture process zone, i.e., the region at which stress concentration ahead of a crevasse tip form microcracks (Pralong, 2006a).

7 Conclusion

Our study sheds light on the relation between ice-related seismicity and the development of gravity-driven glacier instability. Such a relation has been proposed in the past, but simple event detection is inadequate for identification of seismic break-off precursors. On the other hand, an icequake subset, cluster 24, relates to an impending break-off event increasing its activity over similar time scales as the measured frontal acceleration.

The question of whether or not coda wave interferometry introduced here can provide new operational forecast tools has to be addressed with further measurements on different types of hanging glaciers. An enhanced sensor coverage that could be obtained with, for example, a distributed-acoustic sensing (DAS) system deployed at the glacier surface (Walter et al., 2020) would help in resolving the origin and the source mechanism of the multiplets better. Nonetheless, our seismic approach detects dynamic changes involving fracture dislocation within the glacier. This establishes a more direct view of the damage-related processes deep within the glacier than indirect damage manifestation of increased surface velocities captured with radar. Thus, the presented approach constitutes a first-of-its observational constraint on damage growth within unstable glacier ice.

8 Open Research

Obspy Python routines [www.obspy.org, Beyreuther et al. (2010)] were used to download waveforms and pre-process seismic data. REDPY can be downloaded from: `https://github.com/ahotovec/REDPy/`, and FMF from `https://github.com/beridel/fast_matched_filter/` . For source displacement, we used a modified MATLAB code package from Singh et al. (2019). The original MATLAB code package is available at `https://github.com/JonathanSingh/cwi_codes/` .

Seismometer data from stations EIG1, EIG2, EIG3, and EIG4 of the 4D local glacier seismology network (SED, 1985), `http://networks.seismo.ethz.ch/networks/4d/` are archived at the Swiss Seismological Service `http://www.fdsn.org/networks/detail/4D_1985/` .

Interferometric radar data supporting this research are described in Margreth et al. (2017) and are available through the GRAVX online data portal of the company Geoprevent `https://data.geoprevent.com` with restrictions that include confidentiality agreement and are not accessible to the public or research community. To gain access, please contact Lorenz Meier (lorenz.meier@geoprevent.com) or info@geoprevent.com.

Acknowledgments

This work was funded by the Swiss National Science Foundation (SNSF) project Glacial Hazard Monitoring with Seismology (GlaHMSeis, grant PP00P2 157551). We thank John Clinton, Roman Racine, and Stefan Wiemer; the Swiss Seismological Service and its electronic laboratory (ELAB) for technical support and data archiving. We thank Geoprevent Ltd for allowing us to use their high quality radar data and images. We thank Dominik Gräff, Amandine Sergeant, Andrew Curtis, Aurélien Mordret, and Guillaume Jouvet for helpful discussions.

References

Aki, K., & Chouet, B. (1975). Origin of coda waves: source, attenuation, and scattering effects. *Journal of geophysical research*, *80*(23), 3322–3342.

Allen, R. V. (1978). Automatic earthquake recognition and timing from single traces. *Bulletin of the Seismological Society of America*, *68*(5), 1521–1532.

Allstadt, K., & Malone, S. (2014). Swarms of repeating stick-slip icequakes triggered by snow loading at Mount Rainier volcano. *J. Geophys. Res. Earth Surface*, *119*, 1180–1203.

Anandakrishnan, S., & Bentley, C. R. (1993). Micro-earthquakes beneath Ice Streams B and C, West Antarctica: Observations and implications. *J. Glaciol.*, *39*(133), 455–462.

Aster, R., & Winberry, J. (2017). Glacial seismology. *Reports on Progress in Physics*, *80*(12), 126801.

Baggeroer, A. B., Kuperman, W. A., & Mikhalevsky, P. N. (1993). An overview of matched field methods in ocean acoustics. *IEEE J. Oceanic Eng.*, *18*(4), 401-424.

Beaucé, E., Frank, W. B., & Romanenko, A. (2018). Fast Matched Filter (FMF): An Efficient Seismic Matched-Filter Search for Both CPU and GPU Architectures. *Seismological Research Letters*, *89*(1), 165–172. doi: 10.1785/0220170181

Beyreuther, M., Barsch, R., Krischer, L., Megies, T., Behr, Y., & Wassermann, J. (2010, 05). ObsPy: A Python Toolbox for Seismology. *Seismological Research Letters*, *81*(3), 530-533. Retrieved from `https://doi.org/10.1785/gssrl.81.3.530` doi: 10.1785/gssrl.81.3.530

Bowden, D. C., Sager, K., Fichtner, A., & Chmiel, M. (2020, 11). Connecting beamforming and kernel-based noise source inversion. *Geophysical Journal International*, *224*(3), 1607-1620. Retrieved from `https://doi.org/10.1093/gji/ggaa539` doi: 10.1093/gji/ggaa539

Caplan-Auerbach, J., & Huggel, C. (2007). Precursory seismicity associated with frequent, large ice avalanches on iliamna volcano, alaska, usa. *Journal of Glaciology*, *53*(180), 128–140. doi: 10.3189/172756507781833866

Chiaraluce, L., Di Stefano, R., Tinti, E., Scognamiglio, L., Michele, M., Casarotti, E., ... Marzorati, S. (2017). The 2016 Central Italy Seismic Sequence: A First Look at the Mainshocks, Aftershocks, and Source Models. *Seismological Research Letters*, *88*(3), 757–771.

Chmiel, M., Roux, P., & Bardainne, T. (2019). High-sensitivity microseismic monitoring: Automatic detection and localization of subsurface noise sources using matched-field processing and dense patch arrays. *GEOPHYSICS*, *84*(6), KS211-KS223. doi: 10.1190/geo2018-0537.1

Chmiel, M., Roux, P., Herrmann, P., Rondeleux, B., & Wathelet, M. (2018). Data-based diffraction kernels for surface waves from convolution and correlation processes through active seismic interferometry. *Geophysical Journal International*, *214*(2), 1468-1480. Retrieved from `https://doi.org/10.1093/gji/ggy211` doi: 10.1093/gji/ggy211

Colgan, W., Rajaram, H., Abdalati, W., McCutchan, C., Mottram, R., Moussavi, M. S., & Grigsby, S. (2016). Glacier crevasses: Observations, models, and mass balance implications. *Reviews of Geophysics*, *54*(1), 119-161. doi: https://doi.org/10.1002/2015RG000504

Cuffey, K. M., & Paterson, W. S. B. (2010). *The physics of glaciers.* Academic Press.

Curtis, A., Gerstoft, P., Sato, H., Snieder, R., & Wapenaar, K. (2006). Seismic interferometry—turning noise into signal. *The Leading Edge*, *25*(9), 1082–1092.

Dalban Canassy, P., Faillettaz, J., Walter, F., & Huss, M. (2012). Seismic activity and surface motion of a steep temperate glacier: a study on triftgletscher, switzerland. *Journal of Glaciology*, *58*(209), 513–528. doi: 10.3189/2012JoG11J104

Dalban Canassy, P., Walter, F., Husen, S., Maurer, H., Faillettaz, J., & Farinotti, D. (2013). Investigating the dynamics of an alpine glacier using probabilistic icequake locations: Triftgletscher, switzerland. *Journal of Geophysical Research: Earth Surface*, *118*(4), 2003–2018.

Danesi, S., Bannister, S., & Morelli, A. (2007). Repeating earthquakes from rupture of an asperity under an antarctic outlet glacier. *Earth and Planetary Science Letters*, *253*(1), 151-158. Retrieved from `https://www.sciencedirect.com/science/article/pii/S0012821X0600745X` doi: https://doi.org/10.1016/j.epsl.2006.10.023

Deichmann, N., Ansorge, J., Scherbaum, F., Aschwanden, A., Bernard, F., & Gudmundsson, G. (2000). Evidence for deep icequakes in an alpine glacier. *Annals of Glaciology*, *31*, 85–90.

Faillettaz, J., A., P., M., F., & N., D. (2008). Evidence of log-periodic oscillations and increasing icequake activity during the breaking-off of large ice masses. *Journal of Glaciology*, *54*(187), 725–737. doi: 10.3189/002214308786570845.

Faillettaz, J., Funk, M., & Sornette, D. (2011). Icequakes coupled with surface displacements for predicting glacier break-off. *Journal of Glaciology*, *57*(203), 453–460. doi: 10.3189/002214311796905668

Faillettaz, J., Funk, M., & Vincent, C. (2015). Avalanching glacier instabilities: Review on processes and early warning perspectives. *Rev. Geophys.*, *53*, 203-224.

Faillettaz, J., Sornette, D., & Funk, M. (2011). Numerical modeling of a gravity-driven instability of a cold hanging glacier: reanalysis of the 1895 break-off of altelsgletscher, switzerland. *Journal of Glaciology*, *57*(205), 817–831.

Flotron, A. (1977). Movement studies on a hanging glacier in relation with an ice avalanche. *Journal of Glaciology*, *19*(81), 671–672.

Gibbons, S. J., & Ringdal, F. (2006). The detection of low magnitude seismic events using array-based waveform correlation. *Geophys. J. Int.*, *165*(1), 149–166.

Gräff, D., & Walter, F. (2021). Changing friction at the base of an alpine glacier. *Sci Rep*, *11*, 10872. doi: 10.1038/s41598-021-90176-9

Helmstetter, A., Moreau, L., Nicolas, B., Comon, P., & Gay, M. (2015). Intermediate-depth icequakes and harmonic tremor in an alpine glacier (glacier d'argentière, france): Evidence for hydraulic fracturing? *Journal of Geophysical Research: Earth Surface*, *120*(3), 402–416.

Helmstetter, A., Nicolas, B., Comon, P., & Gay, M. (2015). Basal icequakes recorded beneath an alpine glacier (glacier d'argentière, mont blanc, france): Evidence for stick-slip motion? *Journal of Geophysical Research: Earth Surface*, *120*(3), 379–401.

Hotovec-Ellis, A., & Jeffries, C. (2016). Near Real-time Detection, Clustering, and Analysis of Repeating Earthquakes: Application to Mount St. Helens and Redoubt Volcanoes. In *Presented at seismological society of america annual meeting.*

Huss, M., Voinesco, A., & Hoelzle, M. (2013). Implications of climate change on glacier de la plaine morte, switzerland. *Geographica Helvetica*, *68*(4), 227–237. Retrieved from `https://gh.copernicus.org/articles/68/227/2013/` doi:

10.5194/gh-68-227-2013

Kuperman, W. A., & Turek, G. (1997). Matched field acoustics. *Mechanical Systems and Signal Processing*, *11*, 141-148.

Lüthi, M. P., & Funk, M. (1997). Wie stabil ist der hängegletscher am eiger? *Spektrum der Wissenschaft*, *5*, 21–24.

Marchetti, E., Walter, F., & Meier, L. (2021). Broadband infrasound signal of a collapsing hanging glacier. *Geophysical Research Letters*, *48*(16), e2021GL093579.

Margreth, S., Funk, M., Tobler, D., Dalban, P., Meier, L., & Lauper, J. (2017). Analysis of the hazard caused by ice avalanches from the hanging glacier on the eiger west face. *Cold Regions Science and Technology*, *144*, 63-72. (International Snow Science Workshop 2016 Breckenridge) doi: https://doi.org/10.1016/j.coldregions.2017.05.012

Meier, L., Jacquemart, M., Blattmann, B., Wyssen, S., Arnold, B., & Funk, M. (2016). Radar-based Warning and Alarm Systems for Alpine Mass Movements. In *Proceedings of the 13th interpraevent congress* (p. 960–968).

Mikesell, T. D., van Wijk, K., Haney, M. M., Bradford, J. H., Marshall, H. P., & Harper, J. T. (2012). Monitoring glacier surface seismicity in time and space using rayleigh waves. *Journal of Geophysical Research: Earth Surface*, *117*(F2). Retrieved from https://agupubs.onlinelibrary.wiley.com/doi/abs/10.1029/2011JF002259 doi: https://doi.org/10.1029/2011JF002259

Nanni, U., Gimbert, F., Vincent, C., Gräff, D., Walter, F., Piard, L., & Moreau, L. (2020). Quantification of seasonal and diurnal dynamics of subglacial channels using seismic observations on an alpine glacier. *The Cryosphere*, *14*(5), 1475–1496.

Podolskiy, E., & Walter, F. (2016). Cryo-seismology. *Reviews of Geophysics*.

Poupinet, G., Ellsworth, W. L., & Frechet, J. (1984). Monitoring velocity variations in the crust using earthquake doublets: An application to the calaveras fault, california. *Journal of Geophysical Research: Solid Earth*, *89*(B7), 5719-5731. doi: https://doi.org/10.1029/JB089iB07p05719

Pralong, A. (2006a). Ductile crevassing. *Glacier science and environmental change*, 317-318.

Pralong, A. (2006b). Oscillations in critical shearing, application to fractures in glaciers. *Nonlinear Processes in Geophysics*, *13*(6), 681–693. Retrieved from https://npg.copernicus.org/articles/13/681/2006/ doi: 10.5194/npg-13-681-2006

Pralong, A., & Funk, M. (2005). Dynamic damage model of crevasse opening and application to glacier calving. *Journal of Geophysical Research: Solid Earth*, *110*(B1). Retrieved from https://agupubs.onlinelibrary.wiley.com/doi/abs/10.1029/2004JB003104 doi: https://doi.org/10.1029/2004JB003104

Pralong, A., & Funk, M. (2006). On the instability of avalanching glaciers. *Journal of Glaciology*, *52*(176), 31–48. doi: 10.3189/172756506781828980

Pralong, A., Funk, M., & Lüthi, M. P. (2003). A description of crevasse formation using continuum damage mechanics. *Annals of Glaciology*, *37*, 77–82.

Preiswerk, L. (2018). *Monitoring and structural studies with glacier seismology* (Doctoral dissertation, ETH Zurich, Zurich). doi: 10.3929/ethz-b-000300505

Preiswerk, L., Walter, F., Anandakrishnan, S., Barfucci, G., & others. (2016). Monitoring unstable parts in the ice-covered weissmies northwest face. In *13th congress interpraevent 2016.*

Raymond, M., Wegmann, M., & Funk, M. (2003). *Inventar gefährlicher gletscher in der schweiz, mitteilungen versuchsanstalt für wasserbau, hydrologie und glaziologie der eidgenössischen technischen hochschule zürich, vol. 182, versuchsanstalt für wasserbau.* ETH Zürich: Hydrologie und Glaziologie.

Röthlisberger, H. (1972). *Seismic exploration in cold regions.* Hanover: Cold Regions Research and Engineering Laboratory.

Röthlisberger, H. (1977). Ice avalanche. *Journal of Glaciology*, *19*(81), 669–671. doi: 10.3198/1977JoG19-81-669-671

SED. (1985). *Temporary deployments in Switzerland associated with glacier monitoring; ETH Zurich. Other/Seismic Network* [dataset]. Swiss Seismological Service (SED) at ETH Zurich. Retrieved from `https://doi.org/10.12686/sed/networks/4d` doi: doi.org/10.12686/sed/networks/4d

Sens-Schönfelder, C., & Brenguier, F. (2019). Noise-based monitoring. In N. N., L. Gualtieri, & A. Fichtner (Eds.), *Seismic Ambient Noise* (p. 267-301). Cambridge University Press.

Sergeant, A., Chmiel, M., Lindner, F., Walter, F., Roux, P., Chaput, J., ... Mordret, A. (2020). On the green's function emergence from interferometry of seismic wave fields generated in high-melt glaciers: implications for passive imaging and monitoring. *The Cryosphere*, *14*(3), 1139–1171. doi: 10.5194/tc-14-1139-2020

Singh, J., Curtis, A., Zhao, Y., Cartwright-Taylor, A., & Main, I. (2019). Coda wave interferometry for accurate simultaneous monitoring of velocity and acoustic source locations in experimental rock physics. *Journal of Geophysical Research: Solid Earth*, *124*(6), 5629-5655. Retrieved from `https://agupubs.onlinelibrary.wiley.com/doi/abs/10.1029/2019JB017577` doi: https://doi.org/10.1029/2019JB017577

Smith, A. M. (2006). Microearthquakes and subglacial conditions. *Geophys. Res. Lett.*, *33*, L24501. doi: 10.1029/2006GL028207

Snieder, R., Grêt, A., Douma, H., & Scales, J. (2002). Coda wave interferometry for estimating nonlinear behavior in seismic velocity. *Science*, *295*(5563), 2253–2255.

Thelen, W. A., Allstadt, K., De Angelis, S., Malone, S. D., Moran, S. C., & Vidale, J. (2013). Shallow repeating seismic events under an alpine glacier at Mount Rainier, Washington, USA. *J. Glaciol.*, *59*(214), 345–356.

Tian, L., Yao, T., Gao, Y., Thompson, L., Mosley-Thompson, E., Muhammad, S., ... Li, Z. (2017). Two glaciers collapse in western Tibet. *Journal of Glaciology*, *63*(237), 194–197. doi: 10.1017/jog.2016.122

Tibshirani, R. (1996). Regression shrinkage and selection via the lasso. *Journal of the Royal Statistical Society (Series B)*, *58*, 267-288.

Uchida, N., & Bürgmann, R. (2019). Repeating earthquakes. *Annual Review of Earth and Planetary Sciences*, *47*(1), 305-332. Retrieved from `https://doi.org/10.1146/annurev-earth-053018-060119` doi: 10.1146/annurev-earth-053018-060119

Van der Veen, C. (1998). Fracture mechanics approach to penetration of surface crevasses on glaciers. *Cold Regions Science and Technology*, *27*(1), 31–47.

Wake, L., & Marshall, S. (2015). Assessment of current methods of positive degree-day calculation using in situ observations from glaciated regions. *Journal of Glaciology*, *61*(226), 329–344. doi: 10.3189/2015JoG14J116

Walter, F., Gräff, D., Lindner, F., Paitz, P., Köpfli, M., Chmiel, M., & Fichtner, A. (2020). Distributed acoustic sensing of microseismic sources and wave propagation in glaciated terrain. *Nat Commu*, *2436*. doi: 10.1038/s41467-020-15824-6

Weaver, C. S., & Malone, S. D. (1979). Seismic evidence for discrete glacier motion at the rock–ice interface. *Journal of Glaciology*, *23*(89), 171–184. doi: 10.3189/S0022143000029816

Zoet, L. K., Anandakrishnan, S., Alley, R. B., Nyblade, A. A., & Wiens, D. A. (2012). Motion of an Antarctic glacier by repeated tidally modulated earthquakes. *Nature Geoscience*, *5*(9), 623–626.

Supporting Information for Seismic constraints on damage growth within an unstable hanging glacier

Małgorzata Chmiel[1,2], Fabian Walter[1,2], Antoine Pralong[2], Lukas Preiswerk[2],

Martin Funk[2], Lorenz Meier[3], Florent Brenguier[4]

[1]Swiss Federal Institute for Forest, Snow and Landscape Research WSL, Zürich, Switzerland

[2]Laboratory of Hydraulics, Hydrology and Glaciology (VAW), ETH Zürich, Zürich, Switzerland

[3]Geoprevent AG, Technoparkstrasse 1, Zürich, Switzerland

[4]Univ. Grenoble Alpes, Institut des Sciences de la Terre, Grenoble, France

Contents of this file

Introduction

This file contains supplement text, figures, and a for the manuscript "Seismic constraints on damage growth within an unstable hanging glacier". Supplemental Text 2 describes the study site, the Eiger hanging glacier in Switzerland. Supplemental Text 2 provides a detailed description of methods used in this study. Supplemental Text 3 provides additional information on the analytical model of glacier front velocity that is presented in the main manuscript.

Supplemental Figure S1 shows a 2D section of the Eiger hanging glacier. Figure S2 shows hourly time series of: the maximum velocity of the glacier front, icequake occurrence, and air temperature. Figure S3 shows seismograms of icequake multiplets for different clusters. Figure S4 shows Matched Field Processing (MFP) results. Figure S5 shows icequake seismograms from Rhone glacier and Eiger hanging glacier. Figure S6 shows source displacements measured at station EIG2 and EIG4. Figure S7 shows the coda wave interferometry (CWI) measurements of relative seismic velocity variations (dv/v) and the measurement of the coda wave attenuation Q_c. Figure S8 and S9 show the results of the frontal velocity calculated with analytical models. Figure S10 illustrates different perturbation types and their imprint on coda waves. Figure S11 shows a lateral view of the glacier from an automatic camera photographing the unstable ice mass. Supplemental Table S1 provides the values of parameters used to calculate analytically the frontal velocity of the Eiger hanging glacier.

Text S1. The Eiger hanging glacier

The only study that performed thermal, depth, and flow measurements on the Eiger hanging glacier dates back to 1997 (Lüthi & Funk, 1997; Margreth et al., 2017). In a field campaign lasting several days in the spring of 1993, Lüthi and Funk (1997) determined the glacier's thickness by using a ground-penetrating radar along several longitudinal and transverse profiles. In addition, seven boreholes were drilled in the glacier up to 70 m with hot-water drilling. The temperature of the glacier was determined using thermistors installed in the boreholes. 15 stakes were drilled into the ice as reference points, and their position was measured several times with an interval of three weeks to determine the flow velocity on the surface. Based on those measurements and using the finite element method, Lüthi and Funk (1997) provided a glacier model to determine the flow lines of the ice as well as the temperature and stress distribution in the hanging glacier (Figure S1). Their results show that the coldest area is on the glacier bed close to the unstable front. This may be surprising at first, but the glacier location might explain it. The shady location of the glacier front ensures low temperature, and the ice cools down from the front. The rock underneath is often snow-free and transfers the cold to the glacier bed. As a result, the ice in the glacier front is frozen to the ground, contributing significantly to the glacier's stability.

Text S2. Methods

1. **Seismic activity analysis**

We use short time average (STA) long time average (LTA) algorithm e.g., Allen (1978) to evaluate the icequake activity at the Eiger hanging glacier. The STA/LTA algorithm continuously averages the absolute amplitude of a seismic signal in two consecutive moving time windows. Long time window (LTA) is sensitive to changing seismic noise and the short time window (STA) provides information about seismic events. When the ratio of both exceeded a pre-set value, an event is declared. Following Preiswerk (2018), we combine two sets of parameters sta=0.2 s and lta= 5s, sta=0.08 s and lta=0.8 s to detect different types of events, and thresholds 5 and 2 for trigger on and off. We use coincidence triggering to avoid local artifacts, meaning that the event has to be recorded on 4 channels (2 stations). We also account for changing trigger sensitivity by leaving out low amplitude events (Walter et al., 2008), with median amplitude of events <2e-7 m s^{-1}. We do so because the sensitivity of detection changes diurnally and seasonally depending on the number of working stations and different noise levels when the surface melt starts on the glacier. The daily icequake occurrence rate for the entire monitoring period (April 14-August 31, 2016) is presented in Figure S2 together with the maximum velocity of the glacier front and daily temperatures. For additional details of icequake activity on the Eiger glacier, we refer the reader to Preiswerk (2018).

2. Repeating icequakes: RedPy

We use RedPy (A. Hotovec-Ellis & Jeffries, 2016) to investigate the occurrence of repeating icequakes between August 12 and 31, 2016. The RedPy detector runs on seismic data recorded at stations EIG2 and EIG4 (the data are high-pass filtered at 1 Hz). RedPy first runs an STA/LTA triggering algorithm and then a clustering algorithm based on cross-correlations. A cluster contains all events that correlate with at least one other event in the cluster above the correlation threshold. Clusters can combine if a new event correlates with an event in two or more clusters. We use similar settings in RedPY as for the STA/LTA: 4 channels need to be triggered in STA/LTA, we use 6 channels in total (2 stations), lta= 5, sta= 0.2, trigon= 5, trigoff= 2. The cross-correlation threshold of 0.9 has to be exceeded on 4 channels for an event to be counted.

3. **Icequake multiplets: template matching**

To complete the repeater catalog, we perform a template matching over the entire monitoring period. 30 clusters are selected that show the highest number of repeaters (between ∼40 and ∼500). We exclude one cluster with a unusual high number of detected repeaters (>900). We first define templates by stacking icequake signals per cluster. The templates are cross-correlated with continuous signals recorded at the EIG2 station. This is the only station that was operational for the entire monitoring period. We use Fast Matched Filter [FMF, (Beaucé et al., 2018)] for the implementation. FMF first computes normalized cross-correlations between a template and a sliding time window for each signal component and then the average correlations over the three components. We consider a correlation peak as a possible detection if the correlation exceeds 0.7. Icequake waveforms are rather simple due to the homogeneity of glacier ice. Using a too low threshold coefficient with a single station might cause the detection of events that do not belong to the same cluster. Therefore, we chose to work with the cross-correlation coefficient of 0.7, which is low enough to complete the repeater analysis over the extended period but also high enough to reject events that originated from different clusters.

FMF returns the time series of the average correlation coefficients (CC) calculated for each template. The sliding time windows are taking every sample. We group the detections within the time window of +/-1.5 template length, and then we keep only the highest correlation coefficients to avoid double detections. Moreover, we cross-check detections for all clusters to eliminate double detections by keeping the detections in the cluster with the highest cross-correlation coefficient. Figure S3 shows vertical ground velocities of individual icequakes, their stacks, and amplitude spectra of the stack for each cluster.

4. **Matched-Field Processing**

Following Chmiel, Roux, and Bardainne (2019) we Matched-Field Processing (MFP) to localize the clusters. The MFP output value is normalized between 0 and 1 due to the normalization of the the cross-spectral correlation matrix (CSDM) and the wave propagation model. We use the MFP output value to optimize the Rayleigh phase velocity, which is the result of the grid search over northing, easting, and phase velocity in the range 1550-1700 m s^{-1} (spatial and velocity increments of 1 m, and 10 m s^{-1}, respectively). MFP uses the entire icequake waveform (0-1.5 s time window), assuming a 2-D Rayleigh wave propagation. The optimal velocity is found as the one that maximizes the MFP output. The averaging over all optimized phase velocities per cluster while rejecting the results with border velocity values (1550 and 1700 m s^{-1}) gives an average Rayleigh wave phase velocity of 1612 m s^{-1}. This velocity is then used for the calculation of the final MFP output maps. Since the number of stations is limited (2-4) and the clusters are probably located outside of the array, the ambiguity maps do not reveal focal-spot-like locations but rather the direction for which the match between the model and the data is the highest (Figure S4).

5. **Coda Wave Interferometry**

Usually, icequakes are characterized by limited coda caused by a lack of scatterers in glacier ice. However, highly damaged ice and the geometry of the Eiger hanging glacier generate significant icequake coda (Figure S5). This allows us to use the englacial coda to measure source displacement (δ), velocity variations (dv/v), and coda attenuation (Q_c) using the following processing scheme:

(i) Time-window duration. Coda wave interferometry (CWI) uses later times of seismograms in which the waves are sufficiently scattered to contain waves traveling in many different directions (coda waves). We evaluate a lapse-time dependence of coda decay rate to find out at which time noise becomes stronger than the scattered energy on retrieved icequake seismograms. After visual inspection of the decay of the envelope of the icequake seismograms, we chose the time window used in CWI as T_{max}= 1.5 s, and T_{min}=0.5 s to avoid the influence from ballistic waves.

(ii) Stability enhancement. To enhance the coda's signal-to-noise ratio, we first stack up to 3 events per hour with the highest cross-correlation coefficient obtained from the template matching, and then we further stack the icequake waveforms in regular bins of 4 h (up to 12 events per stack). We use only 3 events per hour to limit the influence of a variable number of events in the stack on the CWI results. Then, to further improve the quality of the input data, we analyze the temporal stability of icequake seismograms by correlating a stack of all icequake seismograms and seismograms stacked in 4-hour time window. If the stack is equivalent to the reference trace, the cross-correlation coefficient should be equal to 1. We then keep only 4-h stacks with cross-correlation coefficients >0.7.

(iii) Source displacement. Following Snieder, Grêt, Douma, and Scales (2002); Singh, Curtis, Zhao, Cartwright-Taylor, and Main (2019) the separation δ in the source location for isotropic sources in a three-dimensional acoustic medium reads:

$$\delta = \frac{1}{3\alpha^2}\sigma_\tau^2 \tag{1}$$

Where: σ_τ^2- the variance of the travel time perturbations, α-an estimate of the velocity in the medium.

For double couple sources with the same source mechanism on the same fault plane in elastic media, the source separation δ can be calculated as:

$$\delta = \frac{7(\frac{2}{\alpha^6} + \frac{2}{\beta^6})}{(\frac{6}{\alpha^8} + \frac{7}{\beta^8})}\sigma_\tau^2 \tag{2}$$

Where: α, β-are estimates of the P and S wave velocities in the medium.

The variance of the travel time perturbations σ_τ^2 can be estimated from:

$$\sigma_\tau^2 = \frac{2(1 - R_{max})}{\omega_\tau^2} \tag{3}$$

Where: ω_τ^2-is the dominant mean square, angular frequency, and R_{max} is the maximum correlation coefficient. The dominant mean square angular frequency is calculated as a ratio of the sum of squares of the temporal derivative of the reference trace and the sum of squares of the reference trace in a sliding time window.

Since we do not know the source mechanism of the icequakes within the clusters, we calculate the source displacement following equation 1. As the velocity, we use the previously optimized Rayleigh velocity with MFP (1612 m s^{-1}). However, we verified that a different source mechanism or different seismic velocities change the magnitude of the source displacement, but not the relative variations over time.

The method operates in subsequent short (here: 3 times the maximum period 0.1 s) sliding windows (overlap=90 %) along the lag time. Following A. J. Hotovec-Ellis, Gomberg, Vidale, and Creager (2014) and Allstadt and Malone (2014) we assume that there is some continuous function of source displacement with time and that each pair of stacked icequake multiplets is sampling the difference between the source displacement at those two times. We solve the continuous function of source displacement that fits all the pairs of observed differential changes by a simple linear least-squares inversion. Because of the stacking process, the shortest time we allow the source to change is 4 h. To optimize the processing time, we estimate the source separation between each 5th stack (taken as a reference) vs. every consequent stack. We do this inversion separately for each component of station EIG2 and each cluster which provides us with 90 measurements of the source displacements. We average the source displacement over 3 components and use the standard deviation as an estimation of the uncertainty. Since our input data from inversion is sparse and the inversion approach that we chose makes us lose the initial information on the absolute values of the source displacement, we do not force the inversion results to be non-negative to avoid highly-biased inversion (Allstadt & Malone, 2014). We, however, apply a constant correction of 3 m to obtain non-negative displacement values. We calculate the source displacement for the station EIG2 (cc>0.7, Figure 3C, cc>0.8, Figure S6A, cc>0.9, Figure S6B) and for the station EIG4 (cc>0.7, Figure S6C).

(iv) Doublet method. We use the doublet method, also called Moving Window Cross Spectral technique (Fréchet et al., 1989; Clarke et al., 2011) to calculate dv/v with the same inversion scheme as described for the source displacement. In each window, dt is assumed to be constant, and the current trace is considered to be a time-shifted version of the reference. For each segment, first, the phase spectra difference is calculated (the phase of the cross spectrum for the reference and the current trace). A linear fit over the cross-spectrum as a function of frequency provides the dt value through the slope and error estimations. The measured dt is assigned to the lapse time at the center of the time window (t). The time differences are calculated at a given time lag, allowing us to assess the dt/t value through the slope. Then, using the relationship for homogeneous velocity change in a medium, (Snieder et al., 2019), we obtain: $dv/v = -dt/t$, where dv/v is the relative velocity variation. The dv/v error is calculated as the error of the ordinary least squares solution to the linear system of equations $t * dt/t = dt$. Figure S7B shows the dv/v measurements averaged over all 30 clusters.

(v) Q estimation. To quantitatively characterize the envelope decay gradient, we use coda attenuation, on the basis of the model by Aki and Chouet (1975): $A(t, T_c) \propto t^{-n}\exp(-\frac{\pi t}{Q_c T_c})$, where A, t, and T_c are envelope amplitude, lapse time and central period, and the power n depends on a geometrical spreading. Multiplying a geometrical spreading factor to the left-hand side and taking log_{10}, we estimate Q_c using linear regression analysis. In the model, we use the body wave geometrical spreading (n=1), although we also tested the surface wave geometrical spreading (n=2). We found the same relative changes in the Q_c with slightly lower Q_c values (a median difference over the whole monitoring period between the two models ΔQ=7). Figure S7C shows the Q_c measurements averaged over all 30 clusters

Text S3. Analytical model of glacier front velocity

We follow an approach from Pralong (2006b) for modeling the glacier front velocity. Pralong and Funk (2005) and Pralong (2005) describe the fracture of the glacier using a shear process assuming a ”strain equivalence principle” (Pralong, 2005) and incompressibility of the damaged ice.

We optimise the n and C values using a grid-search over 100 discrete values in 1-4 (linear scale) and 10^0-10^{17} (logarithmic scale) accordingly. For misfit calculations, we use normalized Root Sum Square (RSS). The results of the optimization indicate the $n = 1.2$ and $C = 5.5$x10^{13}. The misfit function shows a trade-off in between the optimized C and n values.

The choice of damage parameterization and the value of Glen's flow law exponent n significantly influence the shape of the acceleration. Both parameters are uncertain. We also test an alternative damage parameterization where the damage variable D describes the cross-sectional reference area and the reduced cross-sectional area.

$$D = (\frac{\Delta}{\Delta_0})^2 \tag{4}$$

In equation 4 the power of 2 reflects the expected damage growth along a plane that cuts through the ice bridge, whereas the cluster displacement Δ is a distance and thus one-dimensional.

The results of the optimization are shown in Figure S8 D and E. The fit with $n = 1.5$ agrees within 87 % with the measured glacier frontal velocity but shows a lower fit quality for the stable frontal velocity values. We also force $n = 3$ for both damage parameterizations and adjust the C value manually based on the misfit functions in Figure S8A and D. The results are shown in Figure S8C and F. The two models provide reasonable fits to the measured glacier frontal velocities. However, the models diverge ~5 days (Figure S8C) and ~2 days (Figure S8F) before the break off event for $D = \frac{\Delta}{\Delta_0}$ and $D = (\frac{\Delta}{\Delta_0})^2$, respectively.

We also propose an alternative approach to model the frontal glacier velocity that does not rely on the parallel-sided slab approximation and assumes tensile damage. For non-linear viscous ice deformation, the rheological relation between the i^{th} and j^{th} entries of the stress and strain rate tensors, σ_{ij} and $\dot{\epsilon}_{ij}$, can be written as $\sigma_{ij} = -p\delta_{ij} + 2\eta\dot{\epsilon}_{ij}$, where p is the pressure and δ_{ij} is the Kronecker delta function.

η is the viscosity, which for damage-prone ice can be expressed as (Pralong et al., 2003):

$$2\eta = A^{-1/n}(1 - D)^{\frac{n+1}{n}}\Pi_{\dot{\epsilon}}^{\frac{1-n}{2n}} \tag{5}$$

where A and n are the flow parameters (n is the Glen's flow law exponent), and $\Pi_{\dot{\epsilon}}$ is the second invariant of the strain rate tensor. The longitudinal strain is thus:

$$\dot{\epsilon}_{xx} = C\frac{1}{(1 - D)^{\frac{n+1}{n}}} \tag{6}$$

The factor $C = A^{1/n}\frac{1}{\Pi_{\dot{\epsilon}}^{\frac{1-n}{2n}}}(\sigma_{xx} + p)$ and we assume that it is constant implying that the stresses driving the ice mass detachment do not change. If we further describe the frontal velocity by a purely longitudinal stretching and assume that this stretching is constant over a length scale L, then the frontal velocity can be approximated by multiplying equation 6 by this length scale. Following the common practice of taking $n = 3$ (Cuffey & Paterson, 2010) we can fit this product to the measured velocity with C being the only loose parameter and the damage D expressed by equation 4.

The numerical value of parameter C for equation 6 is $C = 4.5 * 10^{-2}$. Assuming that longitudinal stresses dominate and are on the order of the hydrostatic pressure near the bed (40 m ice thickness) and $A = 5 * 10^{-24}(Pa^{-n}s^{-1})$ (Pralong et al., 2003), the analytic equation of C $\sim 10^{-5}$. Since equation 6 has to be multiplied by a scale L to convert frontal strain rate to velocity, the fitted C is thus within 3-4 orders of magnitudes of the expected value (similarly to the results shown in Figure S8 C, F). The assumption of constant stress is certainly an oversimplification contributing to this discrepancy. Another simplification can be found in our damage parameterized (equation 6): the interpretation in terms of crevasse growth affects a system-wide geometry and thus longer length scales than the mesoscale at which damage is usually defined (Pralong et al., 2003). Although a scaling between damage and cluster displacement is reasonable with the agreement of ~85 %, the exact relation is unknown.

References

Aki, K., & Chouet, B. (1975). Origin of coda waves: source, attenuation, and scattering effects. *Journal of geophysical research*, *80*(23), 3322–3342.

Allen, R. V. (1978). Automatic earthquake recognition and timing from single traces. *Bulletin of the Seismological Society of America*, *68*(5), 1521–1532.

Allstadt, K., & Malone, S. (2014). Swarms of repeating stick-slip icequakes triggered by snow loading at Mount Rainier volcano. *J. Geophys. Res. Earth Surface*, *119*, 1180–1203.

Beaucé, E., Frank, W. B., & Romanenko, A. (2018). Fast Matched Filter (FMF): An Efficient Seismic Matched-Filter Search for Both CPU and GPU Architectures. *Seismological Research Letters*, *89*(1), 165–172. doi: 10.1785/0220170181

Chmiel, M., Roux, P., & Bardainne, T. (2019). High-sensitivity microseismic monitoring: Automatic detection and localization of subsurface noise sources using matched-field processing and dense patch arrays. *GEOPHYSICS*, *84*(6), KS211-KS223. doi: 10.1190/geo2018-0537.1

Clarke, D., Zaccarelli, L., Shapiro, N. M., & Brenguier, F. (2011). Assessment of resolution and accuracy of the moving window cross spectral technique for monitoring crustal temporal variations using ambient seismic noise. *Geophysical Journal International*, *186*(2), 867-882. doi: https://doi.org/10.1111/j.1365-246X.2011.05074.x

Cuffey, K. M., & Paterson, W. S. B. (2010). *The physics of glaciers.* Academic Press.

Fréchet, J., Martel, L., Nikolla, L., & Poupinet, G. (1989). Application of the cross-spectral moving-window technique (csmwt) to the seismic monitoring of forced fluid migration in a rock mass. *International Journal of Rock Mechanics and Mining Sciences & Geomechanics Abstracts*, *26*(3), 221-233. doi: https://doi.org/10.1016/0148-9062(89)91972-4

Helmstetter, A., Nicolas, B., Comon, P., & Gay, M. (2015). Basal icequakes recorded beneath an alpine glacier (glacier d'argentière, mont blanc, france): Evidence for stick-slip motion? *Journal of Geophysical Research: Earth Surface*, *120*(3), 379–401.

Hotovec-Ellis, A., & Jeffries, C. (2016). Near Real-time Detection, Clustering, and Analysis of Repeating Earthquakes: Application to Mount St. Helens and Redoubt Volcanoes. In *Presented at seismological society of america annual meeting.*

Hotovec-Ellis, A. J., Gomberg, J., Vidale, J. E., & Creager, K. C. (2014). A continuous record of intereruption velocity change at mount st. helens from coda wave interferometry. *Journal of Geophysical Research: Solid Earth*, *119*(3), 2199-2214. Retrieved from `https://agupubs.onlinelibrary.wiley.com/doi/abs/10.1002/2013JB010742` doi: https://doi.org/10.1002/2013JB010742

Jones, G., Kulessa, B., Doyle, S. H., Dow, C. F., & Hubbard, A. (2013). An automated approach to the location of icequakes using seismic waveform amplitudes. *Ann. Glaciol.*, *54*(64), 1-9. doi: 10.3189/2013AoG64A07

Lüthi, M. P., & Funk, M. (1997). Wie stabil ist der hängegletscher am eiger? *Spektrum der Wissenschaft*, *5*, 21–24.

Mao, S., Campillo, M., van der Hilst, R. D., Brenguier, F., Stehly, L., & Hillers, G. (2019). High temporal resolution monitoring of small variations in crustal strain by dense seismic arrays. *Geophysical Research Letters*, *46*(1), 128-137. Retrieved from `https://agupubs.onlinelibrary.wiley.com/doi/abs/10.1029/2018GL079944` doi: https://doi.org/10.1029/2018GL079944

Margreth, S., Funk, M., Tobler, D., Dalban, P., Meier, L., & Lauper, J. (2017). Analysis of the hazard caused by ice avalanches from the hanging glacier on the eiger west face.

Cold Regions Science and Technology, *144*, 63-72. (International Snow Science Workshop 2016 Breckenridge) doi: https://doi.org/10.1016/j.coldregions.2017.05.012

Pralong, A. (2005). *On the instability of hanging glaciers* (Unpublished doctoral dissertation). ETH, Zürich, Switzerland.

Pralong, A. (2006a). Ductile crevassing. *Glacier science and environmental change*, 317-318.

Pralong, A. (2006b). Oscillations in critical shearing, application to fractures in glaciers. *Nonlinear Processes in Geophysics*, *13*(6), 681–693. Retrieved from `https://npg.copernicus.org/articles/13/681/2006/` doi: 10.5194/npg-13-681-2006

Pralong, A., & Funk, M. (2005). Dynamic damage model of crevasse opening and application to glacier calving. *Journal of Geophysical Research: Solid Earth*, *110*(B1). Retrieved from `https://agupubs.onlinelibrary.wiley.com/doi/abs/10.1029/2004JB003104` doi: https://doi.org/10.1029/2004JB003104

Pralong, A., Funk, M., & Lüthi, M. P. (2003). A description of crevasse formation using continuum damage mechanics. *Annals of Glaciology*, *37*, 77–82.

Preiswerk, L. (2018). *Monitoring and structural studies with glacier seismology* (Doctoral dissertation, ETH Zurich, Zurich). doi: 10.3929/ethz-b-000300505

Singh, J., Curtis, A., Zhao, Y., Cartwright-Taylor, A., & Main, I. (2019). Coda wave interferometry for accurate simultaneous monitoring of velocity and acoustic source locations in experimental rock physics. *Journal of Geophysical Research: Solid Earth*, *124*(6), 5629-5655. Retrieved from `https://agupubs.onlinelibrary.wiley.com/doi/abs/10.1029/2019JB017577` doi: https://doi.org/10.1029/2019JB017577

Snieder, R. (2004). Extracting the green's function from the correlation of coda waves: A derivation based on stationary phase. *Physical Review E*, *69*(4), 046610.

Snieder, R., Duran, A., & Obermann, A. (2019). Locating velocity changes in elastic media with coda wave interferometry. In *Seismic ambient noise* (p. 188–217). Cambridge University Press. doi: 10.1017/9781108264808.008

Snieder, R., Grêt, A., Douma, H., & Scales, J. (2002). Coda wave interferometry for estimating nonlinear behavior in seismic velocity. *Science*, *295*(5563), 2253–2255.

Walter, F., Deichmann, N., & Funk, M. (2008). Basal icequakes during changing subglacial water pressures beneath gornergletscher, switzerland. *Journal of Glaciology*, *54*(186), 511–521.

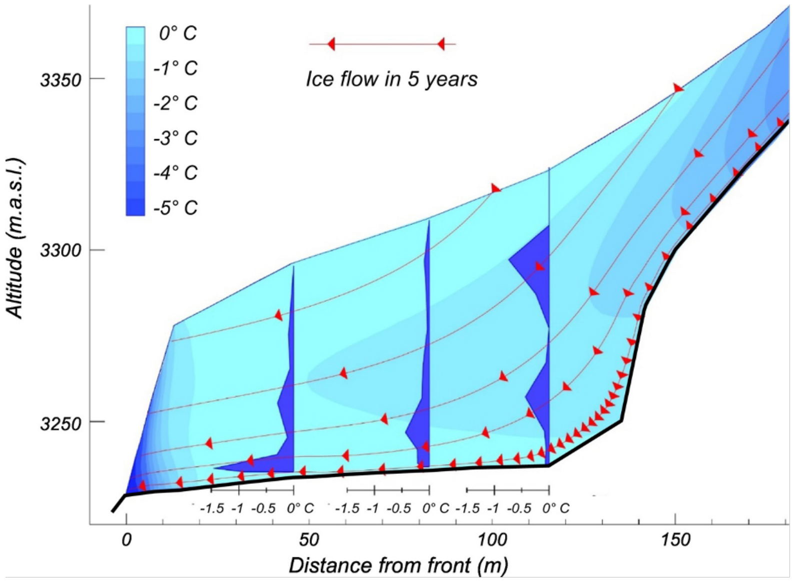

Figure S1. 2D section of Eiger hanging glacier. The cold glacier front (frozen to the glacier bed) is shown on the left side. This ice flow and temperature model was obtained through the finite element method. Englacial ice temperatures measured in three boreholes are also shown (reprinted with permission from Margreth et al. (2017), the original can be found in Lüthi and Funk (1997)).

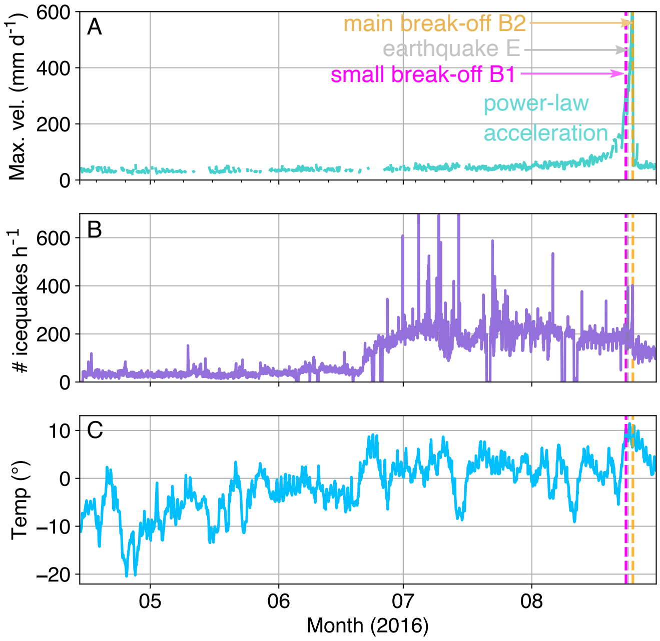

Figure S2. (A) Hourly evolution of the maximum velocity of the glacier front measured from April 15 to August 31, 2016 using an interferometric radar. The maturation of the failure is associated with a power-law acceleration of the glacier front velocity. (B) Hourly icequake occurrence rate: results of the STA/LTA detection algorithm. (c) Air temperature recorded hourly at Jungfraujoch. Small and main break-offs, and Amatrice earthquake (M 6.2) are represented in magenta, gray, and orange dashed vertical bars.

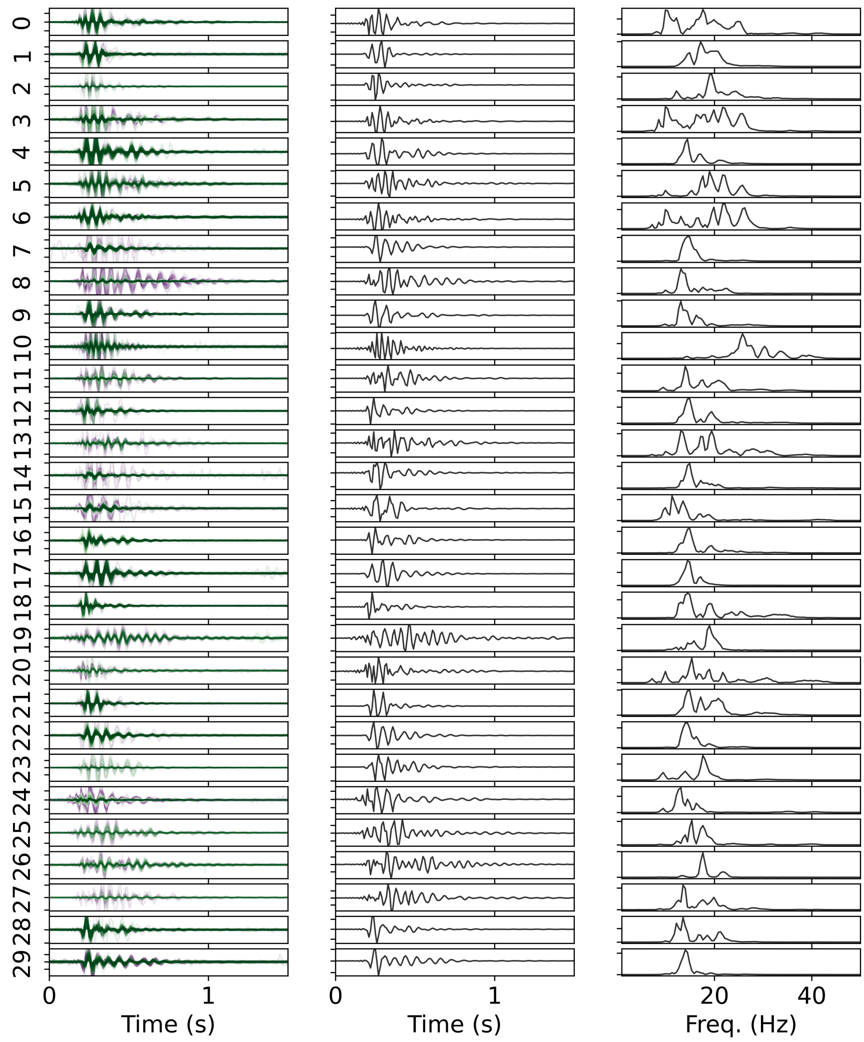

Figure S3. (left) Spaghetti plot of vertical ground velocities from individual icequakes in each cluster, and their stack (middle). (right) Stack amplitude spectrum.

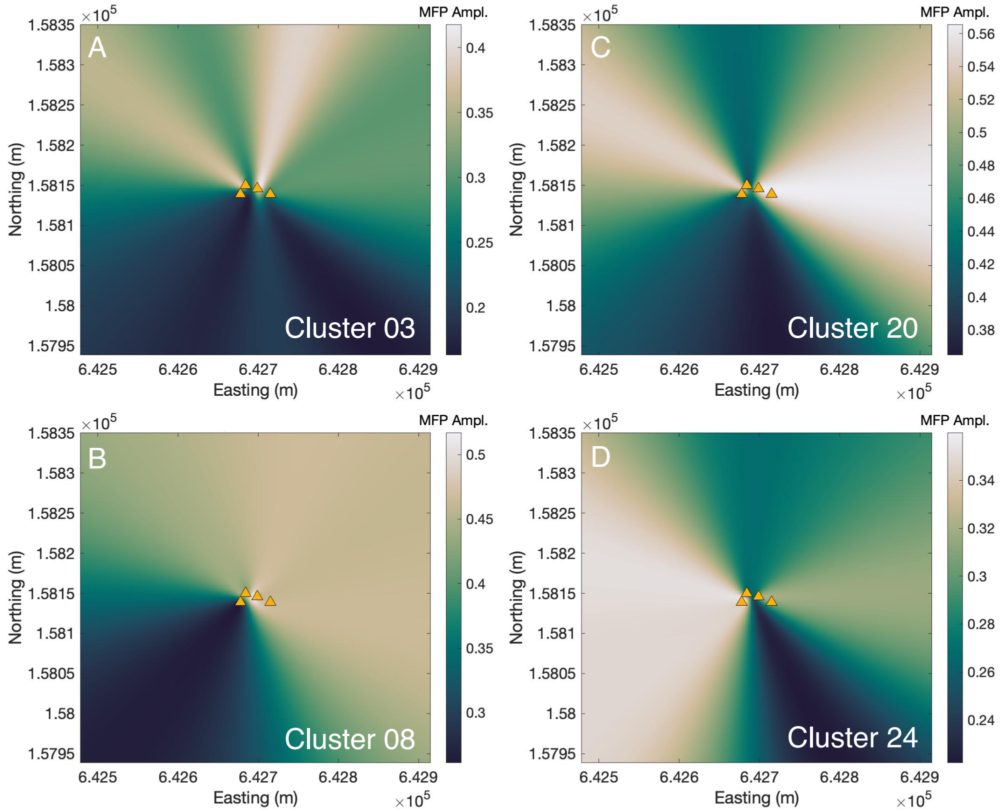

Figure S4. MFP results for cluster (A) 3 (obtained with 4 stations), (B) 8 (obtained with 3 stations), (C), 20 (obtained with 3 stations), and (D) 24 (obtained with 3 stations). The overlaid map in Figure 2A is obtained by stacking the MFP outputs for clusters for which the spatial maximum does not locate at the grid border. The station positions are marked in yellow triangles.

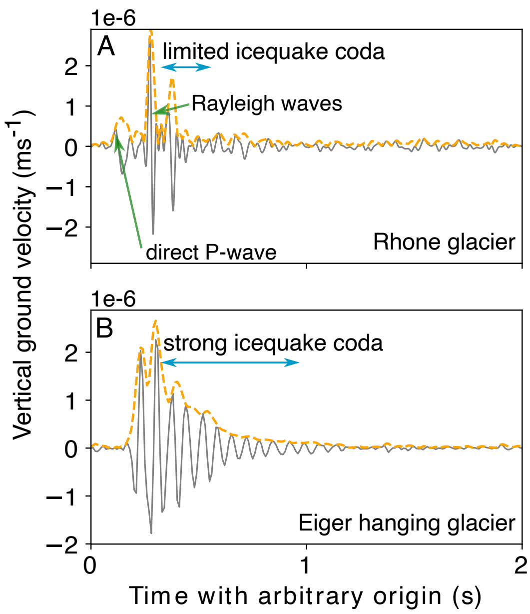

Figure S5. Icequake seismograms from (A) Rhone glacier and (B) Eiger hanging glacier (a single event from cluster 2). On the Rhone glacier, we are able to identify different seismic phases (e.g., direct P-waves and Rayleigh waves). However, on the Eiger hanging glacier, due to the form/shape of the glacier and persisting scattering, the seismic phases are mixed together, which hinders the identification of individual seismic arrivals.

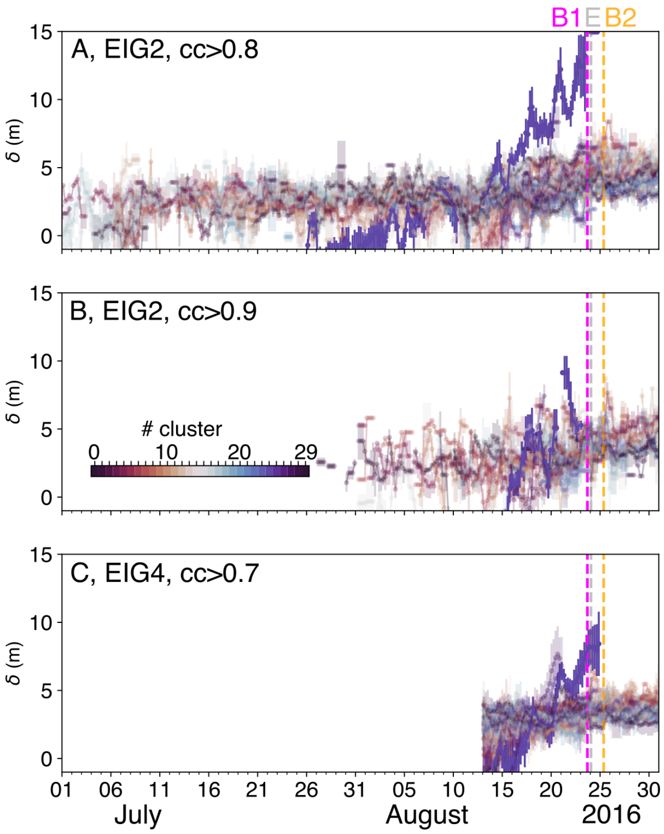

Figure S6. Source displacement δ measured with coda wave interferometry. Source displacement measured at station EIG2 as a function of cross-correlation coefficient used for the icequake multiplet selection (A) cc>0.8, and (B) cc>0.9 (the temporal occurrence of repeaters is too sparse to follow changes in the source displacement). (D) Source displacement measured at station EIG4, cc>0.7. The station EIG4 was installed on August 11, 2016. The small break-off, the earthquake, and the main break-off are shown in 3 dotted lines in pink, gray and orange, respectively.

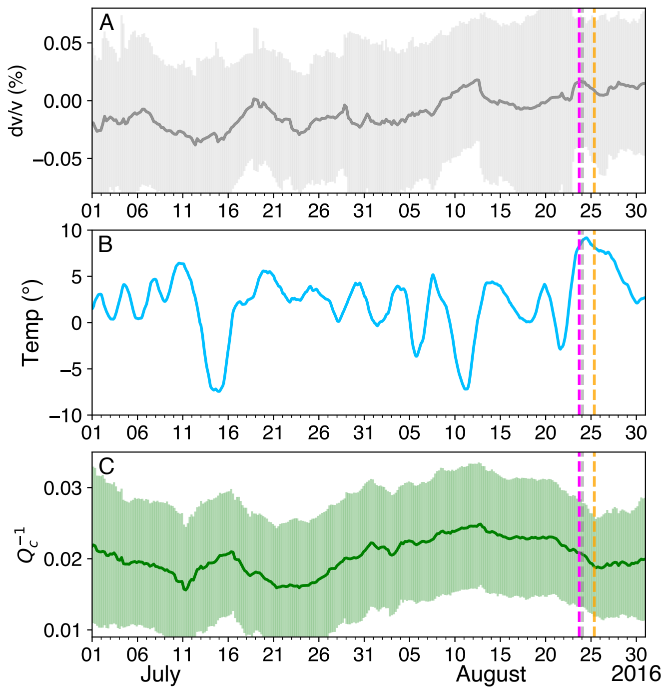

Figure S7. Results of coda wave interferometry (CWI). (A) Averaged dv/v results and its standard deviation, (B) air temperature, (C) averaged coda attenuation Q_c^{-1} and its standard deviation. All measurements are smoothed with a 1-day moving average. Coda-wave interferometry results show weak variations of +/-0.025%(+/-0.05) in relative englacial seismic velocities. Such small dv/v variations can be due to thermal effects (Mao et al., 2019). Singh et al. (2019) showed that source displacement estimates are mostly unaffected by the velocity perturbation. However, velocity change estimates are much more sensitive and might become inaccurate in the presence of larger source perturbations, possibly due to cycle skipping. The seismic quality factor Q_c varies from $\sim$50(+/-25) to Q_c =$\sim$40(+/-25), indicating very high attenuation of seismic waves in the glacier. The Q_c values are similar to previous attenuation estimations for glacial studies with surface waves [Q = 35 at 20 Hz, (Jones et al., 2013) and body waves (Q=20 at 30-500 Hz (Helmstetter et al., 2015)]. The attenuation in the Eiger hanging glacier can be further enhanced by the scattering loss at crevasses. The small break-off, the earthquake, and the main break-off are shown in 3 dotted lines in pink, gray and orange, respectively.

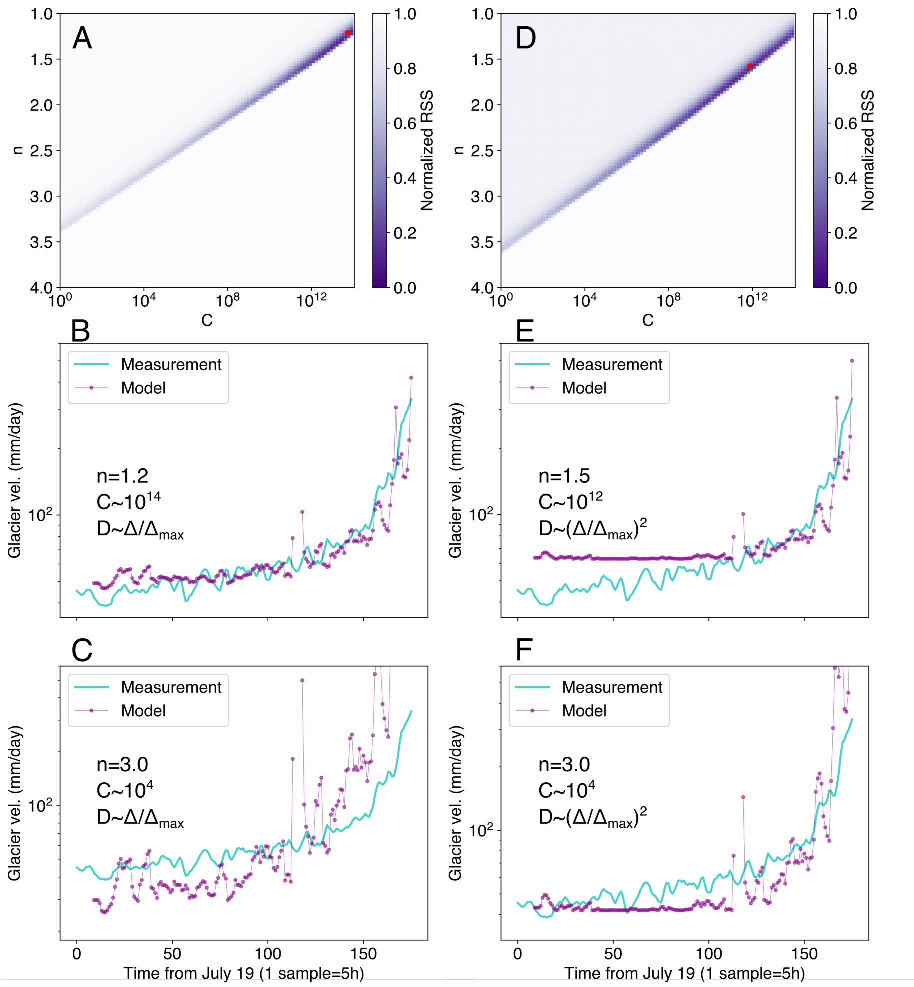

Figure S8. Results of the frontal velocity calculations calculated with the analytical model from Pralong 2005 through the optimization of n and C parameters. A. Normalized RSS calculated using equation 2 and damage parametrization from equation 1 in the main manuscript. B. Model fitted by using optimized parameters. C. Model fitted by forcing n=3 and manually optimizing the C value. D. Normalized RSS calculated using equation 2 in the main manuscript and damage parametrization from equation 4 in SI. E. Model fitted by using optimized parameters. F. Model fitted by forcing n=3 and manually optimizing the C value.

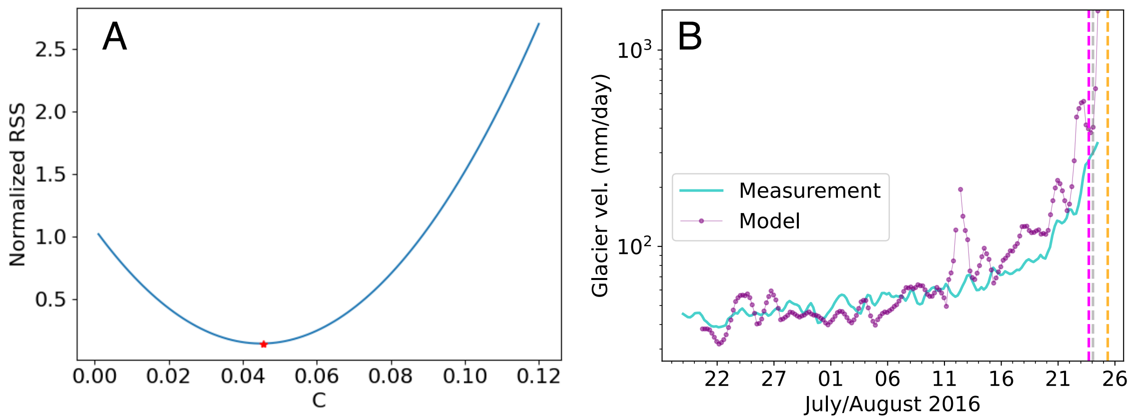

Figure S9. Results of the frontal velocity calculations using the analytical model assuming tensile damage. A. Normalized RSS calculated using equation 6 and damage parameterization from equation 4. B. Model fitted by using optimized parameters.

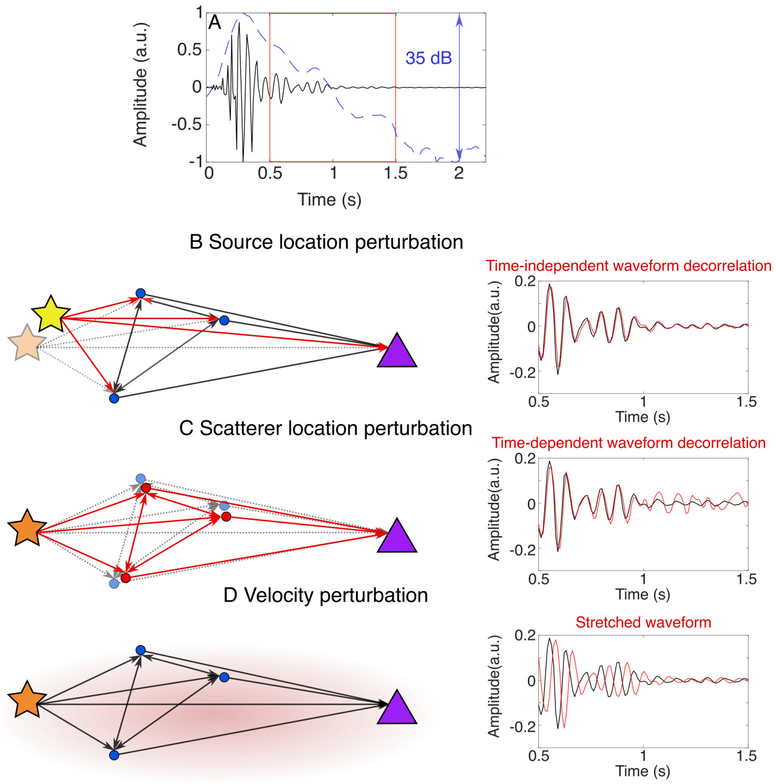

Figure S10. Different perturbation types and their imprint on coda waves (based on Figure 1, Singh et al. (2019)). (A) Stack of all icequakes recorded at the vertical component of the EIG2 station for cluster 24. In red, we show the time window T_{max}= 1.5 s, and T_{min}=0.5 that is used for coda wave interferometry, and in blue, the coda envelope decay in dB. (B, C, and D) Left: the cartoons represent a source (star), receiver (triangle), and a medium with point scatterers (circles). Direct and scattered ray paths are marked in black arrows. Right: the effect on coda waveforms before (black) and after the specific perturbation (red). (B) Source and (C) scatterer location perturbation introduces new ray paths (red arrows) and causes waveform decorrelation. The perturbation in the position of scatterers causes a linear increase in waveform decorrelation with time, whereas for the perturbation of the source position, the waveform decorrelation is independent of time (see Snieder (2004) for details). (D) Homogeneous velocity perturbation in the medium (red radial-gradient) causes stretching of the waveform. Based on Figure 1 in Singh et al. (2019).

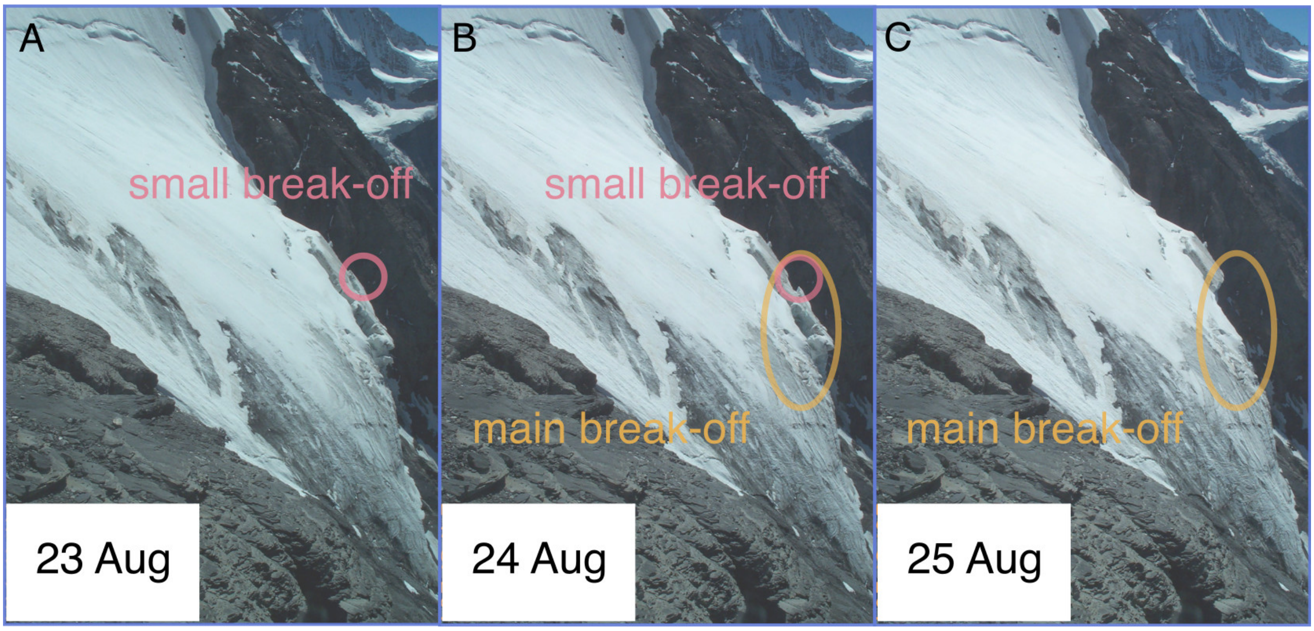

Figure S11. Lateral view of the glacier from an automatic camera photographing the unstable ice mass. (A,B) before the small (23/08/16) and the main break-off event (24/08/16) respectively, and (C) after the break-off event (25/08/16).

A = 5x10^{-24} (Pa^{-n} s^{-1})
b_x = 9.81 sin(45°) (m s^{-2})
H = 40 (m)
ΔH = 10 (m)
ρ = 910 (kg m^{-3})

TableS1. Values of parameters used to calculate analytically the frontal velocity v_x. We use the same values as Pralong (2006b) and for the parameter ΔH (the active layer where damage develops) we use the value of 10 m which is equal at the order of magnitude to the region at which stress concentration ahead of a crevasse tip form microcracks (Pralong, 2006a).